Disruption of CD47-SIRPα signalling restores inflammatory function in tumour-associated myeloid derived suppressor cells

Carlo Zimarino[1], William Moody[1], Sarah E. Davidson[1,2], Hafsa Munir[1,3,4*], Jacqueline D. Shields[1,5,6*]

[1] MRC Cancer Unit, Hutchison/MRC Research Centre, University of Cambridge, UK

[2] The Kennedy Institute of Rheumatology, University of Oxford, Oxford, UK

[3] Helmholtz Institute for Translational Oncology Mainz (HI-TRON Mainz) – A Helmholtz Institute of the DKFZ, Mainz, Germany

[4] German Cancer Research Centre (DKFZ), Heidelberg, Division of Dermal Oncoimmunology, Germany

[5] Comprehensive Cancer Centre, Kings College London, London, UK

[6] Centre for Cancer Sciences, School of Medicine, Biodiscovery Institute, University of Nottingham

* Corresponding Authors: hafsa.munir@dkfz-heidelberg.de and jacqueline.shields@kcl.ac.uk

Summary

Myeloid Derived Suppressor Cells (MDSCs) are a heterogenous immune population with diverse immunosuppressive functions in solid tumours. Here, we explored the role of the tumour microenvironment in regulating MDSC differentiation and immunosuppressive properties via signal-regulatory protein alpha (SIRPα)/CD47 signalling. In a murine melanoma model, we observed progressive increases in monocytic-MDSCs (M-MDSCs) and monocyte-derived dendritic cells (moDCs) that exhibited potent T cell suppressive capabilities. These adaptations could be recapitulated *in vitro* by exposing hematopoietic stem cells to tumour-derived factors. Engagement of CD47 with SIRPα on myeloid cells reduced their phagocytic capability, enhanced expression of immune checkpoints, increased reactive oxygen species production and suppressed T cell proliferation. Perturbation of SIRPα signalling restored phagocytosis and antigen presentation by MDSCs, which was accompanied by renewed T cell activity and delayed tumour growth in multiple solid cancers. These data highlight that therapeutically targeting myeloid functions in combination with immune checkpoint inhibitors could enhance anti-tumour immunity.

Introduction

The advent of immune check point inhibitor (ICIs) therapies that target receptors on T cells, such as CTLA4 and PD-1, to reinvigorate anti-tumour immune responses has changed the landscape of cancer therapy. However, the magnitude and durability of responses varies considerably among patients and tumour types [1-7], with many patients developing therapeutic resistance and experiencing off-target toxicity [8,9]. While T cells are key drivers of anti-tumour immunity and are as such a desirable target for therapeutic intervention, there are a multitude of other infiltrating immune populations within the tumour that play a critical role in tumour progression.

The tumour ecosystem is extremely diverse, rich in myeloid populations including monocytes, macrophages, neutrophils and importantly, dendritic cells (DCs) [10,11]. These innate immune constituents display potent immune modulatory properties through expression of immune regulatory molecules and by presenting antigen. Thus, targeting features of innate immune regulation represents an attractive alternative or synergistic opportunity to improve immune based cancer therapies.

Tumour infiltrating myeloid populations initially display anti-tumour functions, phagocytosing dying tumour cells and presenting antigen to T cells in the draining lymph node. However, as tumours grow, these functions are suppressed, and the cells acquire a pro-tumour phenotype [11-17]. During tumorigenesis, emergency myelopoiesis gives rise to a heterogenous population of myeloid cells termed myeloid-derived suppressor cells (MDSCs). On the molecular level, MDSCs are distinct from mature myeloid cells as they

express key immunosuppressive pathways [18-24]. Much like mature myeloid cells, murine MDSCs can be broadly identified based on expression of common myeloid markers, namely, CD11b and CD11c (which generally distinguish monocytic cells from DCs), as well as Ly6G and Ly6C (which can broadly differentiate monocytes, macrophages and neutrophils)[25,26]. These markers distinguish the two main MDSC subtypes, $CD11c^{-}CD11b^{+}Ly6G^{+}$ granulocytic MDSCs (G-MDSCs) and $CD11c^{-}CD11b^{+}Ly6C^{+}$ monocytic MDSCs (M-MDSCs). While these markers are also commonly expressed by mature myeloid cells, MDSCs are distinguishable because they also exhibit potent T cell suppressive capabilities and in general, are associated with immune suppressive behaviour. Recent single cell sequencing data indicates substantial overlap between the gene signatures of G-MDSCs and M-MDSCs[27], however G-MDSCs are thought to play a critical role in antigen specific ROS-driven T cell-suppression[28] and are prevalent in tumours of prostate and breast. In contrast, M-MDSCs which preferentially accumulate in melanoma, are thought to elicit antigen independent effects via release of Nitric Oxide and Arginase, and production of immune suppressive cytokines. DCs also play a role in tumour progression[29]. Briefly, conventional dendritic cells 1 (cDC1) can activate cytotoxic T cells[30], conventional dendritic cells 2 (cDC2) are key inducers of anti-tumour CD4 T cell responses[31] and monocyte-derived DCs (moDCs) can efficiently induce T_{reg} activation and expansion[32,33]. Therefore, in melanoma, M-MDSCs and moDCs are key contributors to the immune suppressive microenvironment within the growing tumour.

Previous reports have shown that soluble mediators and receptor-antigen interactions within the tumour microenvironment (TME) can skew myeloid functionality to become pro- or anti-tumorigenic depending on the type and stage of disease. Importantly, CD47 expressed by tumour cells has been implicated in the switch in the development and function of the myeloid compartment within tumours. Additionally, CD47 expression by the tumour has been associated with poor prognosis [34,35]. Previous reports have shown that CD47 binds to the immune checkpoint, signal regulatory protein α (SIRPα or CD172a), which is expressed predominantly by myeloid cells. Engagement of SIRPα with CD47 inhibits phagocytosis by myeloid cells. Activation of this pathway has previously been shown to contribute to immune evasion in cancer by limiting clearance of tumour cells by macrophages [36,37]. Engagement of the SIRPα pathway on myeloid populations through CD47 induces phosphorylation of immunoreceptor tyrosine-based inhibition motifs (ITIMs) cytoplasmic domain and activation of the SH2-containing tyrosine phosphatase (SHP-1/2) which in turn mediate an array of inhibitory functions[38,39]. In addition to impairment of phagocytosis, CD47-SIRPα signalling within tumours has also been shown to inhibit DC maturation, antigen presentation, maintenance of MDSC function and prevention of neutrophil migration [40,41].

These observations have led to the development of agents targeting CD47. Its neutralisation has been shown to reduce tumour growth and promote anti-tumour immunity in preclinical tumour models [35,42-44]. The safety and efficacy of these agents is now being tested in clinical trials [45,46]. Reports have shown that CD47 blockade mediates

tumour resolution primarily through increased macrophage clearance [47-49] and via enhanced antigen cross-presentation by DCs which leads to improved T cell priming [43,47]. However, CD47 is ubiquitously expressed in healthy as well as diseased tissue, from tumour cells to erythrocytes, bladder, prostate, fallopian tubes, mediumly in bronchus tissue, salivary glands and sex organs. Thus, its inhibition risks disrupting the function of normal, non-malignant cells, leading to unwanted clinical effects and toxicities such as the induction of anaemia [50-52]. Indeed, clinical trials, including Arch Oncology's phase I/II clinical trial of Ti-061 and Celgene's CC-90002, have been discontinued due to potential toxicity caused by anti-CD47 antibody therapy.

Targeting of SIRPα, the binding partner of CD47, may therefore offer a safer alternative approach with which to modulate myeloid driven anti-tumour immunity, as it's almost exclusively expressed by the myeloid compartment [53]. In support of this, several studies have alluded to enhanced myeloid cell activation post-SIRPα blockade. Indeed, Kuo et al showed that treatment of mice bearing colon cancer with a combination of anti-PD-1/PD-L1 and a chimeric anti-SIRPα neutralising antibody was highly effective in suppressing growth of primary tumours[54]. In this model, anti-SIRPα treatment facilitated monocyte and DC activation and enhanced T cell effector functions. Other studies reported enhanced T cell infiltration post treatment which overcame immunotherapy induced immune exclusion[53]. Furthermore, Zhao et al. showed that blockade of CD47 to interrupt this signalling pathway resulted in enhanced antibody-dependent cellular cytotoxicity of Her2/Neu breast cancer cells by neutrophils after trastuzumab treatment [40]. However, this combination therapy had little efficacy in more aggressive tumour models, such as the B16.F10 melanoma model. Other studies have also highlighted the complexity of SIRPα signalling in the TME and how it may limit therapeutic efficacy although the mechanism is still unclear. Zhou et al recently showed that mice bearing SIRPα-deficient melanomas had no response to anti-PD-L1 treatment, but SIRPα overexpression significantly enhanced immunotherapy response[55]. The discrepancy between colon cancer and melanoma is fascinating and raises several key questions about the role of SIRPα in different tumour contexts and the potential contribution it makes at different stages of tumour evolution.

While T cell immune checkpoints have been well characterised, our understanding of the CD47-SIRPα axis across myeloid populations is less clear. Here, we explore the role of the CD47-SIRPα interactions on myeloid function in a B16.F10 melanoma model. We observed that the myeloid compartment of established tumour primarily consisted of M-MDSCs and moDCs. We confirmed widespread expression of CD47 within the TME while SIRPα expression was limited to myeloid cells. In contrast to Kuo et al., we show that disruption of CD47-SIRPα signalling following selective SIRPα blockade induces energetic rewiring of myeloid cells and is sufficient to slow tumour growth. This is mediated by restoration of phagocytosis, antigen processing and presentation and a shift in CD8:Treg ratios. The effects of SIRPα blockade were not limited to melanoma and translated to other solid tumours, namely pancreatic and breast tumours showing a

conserved anti-phagocytic pathway activated in suppressive myeloid cells across multiple tumour types. Our data indicate that approaches targeting phagocytosis pathways in myeloid populations, boosting antigen uptake and presentation to infiltrating T cells may synergize with conventional immune checkpoint inhibitors and enhance anti-tumour immunity. Therapeutically targeting both innate and adaptive arms may enable the use of lower doses to lower toxicities currently experienced by patients undergoing treatment with T cell targeted immune checkpoint inhibitors or anti-CD47 agents.

Results:

The myeloid compartment dynamically evolves during tumour development.

The presence of distinct myeloid populations in melanoma has been well characterized (extensively reviewed in [25,56]). However, the kinetics of the infiltration and functions of each population as the tumour evolves is less well established. To address this in murine melanoma, we first characterized the myeloid compartment in healthy skin and compared it with the myeloid constituents present in small, palpable skin lesions at 5 days post-tumour induction and at day 9 and 11 post-induction, when tumours were more established (Supplementary Figure 1A). In healthy skin, DCs ($CD11c^+$) and phagocytes ($CD11b^+CD11c^-$) comprised a small proportion of the immune infiltrate. However, early B16.F10 lesions (day 5) exhibited a significant increase in the proportion of both populations, comprising ~80% of the total immune infiltrate compared to healthy skin at day 0 (Figure 1A and Supplementary Figure 1B). The increased phagocyte infiltration was maintained at day 9 and 11 post-induction compared to normal skin (Figure 1A). In contrast, the abundance of DCs decreased sharply as tumours progressed, to a level comparable with phagocytes (Figure 1A and Supplementary Figure 1B). The shift in the dominance of specific myeloid populations may reflect differences in the function of myeloid components as tumours evolve. A more in-depth analysis of specific myeloid populations revealed that monocyte-derived DCs (moDCs; $CD11b^+CD11c^+Ly6C^+$) and monocytic myeloid-derived suppressor cells (M-MDSCs; $CD11b^+CD11c^-Ly6C^+$) both significantly expanded throughout tumour progression compared to healthy skin at day 0 (Figure 1B). However, the M-MDSCs expanded more dramatically than moDCs to become the dominant myeloid population in established day 11 tumours. Surprisingly, the proportion of granulocytic MDSCs (G-MDSCs; $CD11b^+CD11c^-Ly6G^+$) slightly increased as tumours developed but they represented a minor component of the infiltrate compared to M-MDSCs and moDCs (Figure 1B).

We then examined the wider myeloid compartment, observing a decrease in the percentage of cDC1 and cDC2 cells (Supplementary Figure 1B) from day 5 to day 11 post-tumour induction. Within the defined moDC and M-MDSC populations, CX3CR1 marking monocytes and monocyte precursors, and the maturation marker F4/80, used to distinguish macrophages from DCs, were assessed (Supplementary Figure 1C and 1D). Interestingly, approximately 95% of moDC were $F4/80^+$ in day 5 tumours, and this

proportion significantly decreased by Day 11 (Supplementary Figure 1C). Similarly, M-MDSCs also showed a decrease in the proportion of F4/80$^+$ cells in day 11 tumours albeit to a lesser extent than the moDCs. CX3CR1 is expressed by most myeloid constituents and was highly expressed by both moDC and M-MDSCs. Surprisingly, the proportion of CX3CR1$^+$ moDCs slightly increased in day 11 tumours while in M-MDSCs the proportion significantly decreased. These changes in F4/80 and CX3CR1 expression from day 5 to day 11 tumours likely reflects a shift in the phenotype of the moDCs and M-MDSCs to a more immature-like state.

As the recruitment of M-MDSCs and moDCs significantly increased in the evolving tumour, we then sought to understand how they contribute to the changing immune landscape and suppressive microenvironment. By immune phenotyping, we observed an upregulation in the expression of T cell suppressive molecules; PD-L1, FasL and ARG1 across moDC, M-MDSC and G-MDSC subsets from day 5 to day 11 post-tumour induction (Figure 1C). Notably, moDCs were the only population to significantly upregulate NOS2 levels as tumours progressed (Figure 1C), suggesting that while the expression of certain suppressive molecules is shared amongst myeloid populations, cell-type specific phenotypes also exist which may critically influence their function. These data indicate that myeloid populations, particularly moDCs and M-MDSCs, which expand as tumours progress, upregulate T cell suppressive molecules that may contribute to the onset or progression of an immunosuppressive microenvironment within the tumour.

To determine whether acquisition of a suppressive phenotype by these populations translated to a functional inhibition of T cells, we isolated myeloid cells (CD11b$^+$Ly6C$^-$, moDCs and M-MDSCs) from day 11 tumours and co-cultured them with activated CD8 T cells, measuring their proliferative capacity based on CFSE levels (Figure 1D). Co-culture with CD11b$^+$Ly6C$^-$ cells, which includes cDCs and neutrophils, promoted the proliferation of CD8 T cells compared to T cells alone (Figure 1E) which is likely due to their expression of T cell co-stimulatory molecules and their antigen presentation capabilities. In contrast, co-culture with a mixture of moDCs and M-MDSCs significantly suppressed CD8 T cell proliferation compared to CD8 T cells cultured alone or those cultured with the remaining myeloid fraction (Figure 1D and 1E). Importantly, proliferation of CD8 T cells exposed to M-MDSCs were more potently suppressed than those co-cultured with moDCs (Figure 1F and 1G). Interestingly, both populations also impaired CD4 T cell proliferation to comparable levels (Figure 1F and 1G). These data highlight that MDSCs and moDCs which express immunosuppressive markers can functionally suppress both CD4 and CD8 T cell proliferation within the tumour. Of note, the other myeloid components functioned to support T cell proliferation, thus, highlighting that the fine balance of myeloid cells present can determine whether a microenvironment is immunosuppressive or stimulatory. These data support the idea that the tumour promotes a shift in recruitment and phenotype of myeloid populations as tumours develop, towards a more suppressive milieu capable of impairing T cell proliferation.

Tumour conditioning induces myeloid cells to develop a suppressive phenotype.

To model development of suppressive myeloid populations within the tumour and assess whether tumour-derived factors could drive differentiation of myeloid cells towards an immunosuppressive phenotype, we utilized an *in vitro* culture system to generate different myeloid populations from haematopoietic stem cells (HSCs). Briefly, Sca-1$^+$ bone marrow-derived HSCs were cultured in the presence of GM-CSF to maintain their growth, or GM-CSF supplemented with tumour cell conditioned media (GM-CSF+TCM). At Day 0, the culture was predominately composed of HSCs (Sca-1$^+$CD11b$^-$CD11c$^-$, Supplementary Figure 1E) and contained very small proportions of differentiated myeloid cells (Figure 2A and 2B). After 3 days of culture in the presence or absence of tumour-derived factors, the proportion of phagocytes significantly increased compared to normal day 0 cells (Figure 2A, Supplementary Figure 1F) with M-MDSCs comprising the dominant proportion of these cells (Figure 2B). The remaining cells were comprised predominantly of granulocytes, other DC populations and a small proportion of lymphocytes. By day 5 post-differentiation, the cDC fraction had also expanded in both treatment conditions (Figure 2A, Supplementary Figure 1F) and was comprised primarily of moDCs, which also significantly increased compared to normal day 0 cells (Figure 2B). The phagocyte fraction continued to expand up to 5 days of differentiation, largely due to the expansion of M-MDSCs, while the proportion of G-MDSCs remained constant at all time points (Figure 2A and 2B). At this point in the differentiation process, very few HSCs remained (Figure 2A). These data strongly suggest that differentiation of HSCs towards myeloid constituents' favours development of M-MDSCs and moDCs and an absence of G-MDSCs. Furthermore, treatment with tumour-derived factors does not directly influence the differentiation into these cell types in this *in vitro* culture system.

While myeloid composition was unaltered by TCM conditioning *in vitro*, functional alterations were apparent, with moDCs and M-MDSCs derived from TCM-treated HSC cultures capable of suppressing CD4 and CD8 T cell proliferation to a greater extent than those treated with GM-CSF alone (Figure 2C and 2D). In a similar manner to the *in vivo* tumour setting, TCM-treated M-MDSCs, which were the dominant cell type in these cultures, showed increased expression of PD-L1, ARG1 and SIRPα (Figure 2E and supplementary Figure 1G). moDCs showed a slight trend towards increased PD-L1 and SIRPα expression and a significant increase in ARG1 expression following TCM treatment (Figure 2E, Supplementary Figure 1G). In contrast to *in vivo* tumour-derived moDCs and M-MDSCs, FasL was not upregulated upon TCM treatment, suggesting that while the *in vitro* culture system mimics the *in vivo* development of suppressive myeloid populations, the mechanisms that mediate T cell suppression vary between the systems. Furthermore, these data show that tumour-derived factors can enhance the suppressive capability of myeloid constituents without directly influencing their differentiation and development.

The CD47-SIRPα signalling axis drives myeloid cells towards an immunosuppressive phenotype.

We next sought to determine the factors driving the suppressive phenotypes observed in M-MDSCs and moDCs. Previous reports have shown that CD47 binds to SIRPα, an immune checkpoint expressed mainly by myeloid cells. Engagement of these proteins

prevents phagocytosis to limit the clearance of old cells or non-self-antigen presenting cells. In tumours, reports have suggested that once this pathway is triggered, impaired phagocytosis by antigen presenting cells is accompanied by inhibition of their inflammatory activities and impaired clearance of dead or dying cells[35,57]. These previous studies led us to consider whether loss of phagocytosis by engagement of this axis limits the pro-inflammatory, anti-tumourigenic phenotype of moDCs and M-MDSCs to favour suppression of tumour infiltrating T cells.

To test this, we first examined a published scRNA-seq data set[58] characterizing the non-cancer-cell components of the B16.F10 tumour microenvironment (Figure 3A) to determine the distribution of CD47 and SIRPα within the tumour stroma. CD47 was diffusely expressed across both immune and non-immune stromal constituents at the RNA level (Figure 3B and 3C). In contrast, SIRPα expression was more exclusive, restricted to the myeloid, endothelial and immune modulatory cancer-associated fibroblast (CAF) compartments of the tumour (Figure 3B and 3C). CD47 distribution within the TME was confirmed at the protein level in dissociated tumours (Figure 3D). As with RNA, CD47 protein was widely detected across compartments including tumour cells, CAFs, endothelial cells, myeloid and T cells, however, interestingly, the dominant signal within the microenvironment came from T cells[57,59] and immunomodulatory CAFs (CAF1; Figure 3D). SIRPα-expressing cells were predominantly from the myeloid lineage and these SIRPα$^+$ cells were abundant throughout the tumour core (Figure 3E). This suggests that engagement of myeloid cell SIRPα would be predominantly driven via interactions with other stromal components expressing CD47 in addition to those with tumour cells. These data indicate that CD47-SIRPα signalling could be a mechanism contributing to the suppressive effects of myeloid cells within established tumours.

To then determine if CD47-SIRPα signalling plays a role in the acquisition of a suppressive phenotype and mediating immunosuppression, we measured the influence of CD47 stimulation on expression of T cell checkpoint molecules by moDCs and M-MDSCs *in vitro*. Stimulation with active recombinant CD47 peptide (rCD47) augmented the suppressive phenotype of moDC and M-MDSCs compared to GM-CSF, and slightly enhanced the effects of TCM treatment, with elevated expression of PD-L1 FasL, VISTA and IDO (Figure 4A, and Supplementary Figure 2A and 2B). We also observed a significant increase in SIRPα expression by M-MDSC upon CD47 treatment (Figure 4A), indicating that CD47 ligation may operate in a feedback loop to boost SIRPα availability, further sensitizing myeloid cells to CD47 signals and suppressive functions such as inhibition of phagocytosis.

The induction of a more suppressive phenotype through CD47 stimulation was accompanied by an enhanced capacity to inhibit CD8 and CD4 T cell proliferation (Figure 4B). Again, while TCM-treated myeloid populations were more potent than GM-CSF at inhibiting T cell proliferation, this was further augmented following CD47 stimulation and engagement of SIRPα on the MDSCs (Figure 4B). When CD47-SIRPα interactions were disrupted with a SIRPα blocking antibody, any enhanced suppression driven by CD47 engagement was effectively lost (Figure 4B). However, suppression was not fully reversed by α-SIRPα blockade implying that SIRPα sites were not fully occupied, or that other factors also contribute to the suppressive potential of tumour conditioned myeloid

cells. Indeed, a concurrent reduction in PD-L1 and ARG1 expression was detected in mixed moDC and M-MDSC cultures when SIRPα was blocked in the presence of rCD47 compared to CD47 stimulated MDSCs alone (Figure 4C).

Blockade of the CD47-SIRPα interaction restores the phagocytic capabilities of myeloid cells.

Having observed that perturbation of CD47-SIRPα signalling reduced the levels of T cell suppressive molecules and partially restored T cell proliferative potential, we then examined whether blockade of SIRPα signalling also enhanced the phagocytic functions of the myeloid cells. To do this, we modified our *in vitro* system. First, moDCs and M-MDSCs were differentiated in GM-CSF+TCM for 5 days to mimic tumour conditioning. We then incorporated cells found within a tumour which either express high (CAFs) or low (B16.F10 tumour cells) levels of CD47 as determined by flow cytometry (Figure 5A and Supplementary Figure 3A). The cells were fluorescently labelled, and 25% were killed by heat-treatment to generate a mix of live cells and labelled debris. The capacity of moDCs and M-MDSCs to uptake debris in the presence or absence of CD47 was then quantified by flow cytometry (Figure 5B and Supplementary Figure 3B). As expected, both moDC and M-MDSCs displayed enhanced phagocytosis (as measured by fluorescent signal detected within myeloid cells) when in the presence of $CD47^{low}$ tumour cells compared with $CD47^{high}$ CAFs (Figure 5C). Prior to testing whether SIRPα blockade could enhance the phagocytic capacity of moDCs and M-MDSCs, we confirmed that the SIRPα blocking antibody could efficiently bind and occupy all available epitopes. To do this, we performed an antibody competition assay on $Ly6C^{+}$ cells (Supplementary Figure 3C). Briefly, after treatment with the anti-SIRPα blocking antibody, the SIRPα epitope was no longer detectable by conjugated antibodies, indicating that prior treatment with the blocking antibody effectively covered all epitopes and thereby limited detection with the conjugated antibody (Supplementary Figure 4B, left panel). Application of a conjugated anti rat IgG effectively recognised the backbone of the blocking antibody, confirming that it had reached its target, was occupying the SIRPα site and had not been internalised (Supplementary Figure 3C, right panel).

Perturbation of the anti-phagocytic signal induced by SIRPα blockade had little impact on uptake of cellular material by moDCs in the presence of either $CD47^{high}$ or $CD47^{low}$ cells with low doses of SIRPα blocking antibody (Figure 5D). In contrast, even at the lowest concentrations tested, pre-treatment of M-MDSCs with anti-SIRPα significantly boosted their phagocytic capacity (Figure 5E). This may have been a consequence of sub-maximal occupancy by the blocking antibody. Indeed, when titrated, a dose dependent enhancement of phagocytosis on M-MDSCs and moDCs could be detected with increasing concentrations of blocking antibody (Figure 5F).

These data highlight that myeloid cells recruited to the tumour enter at the periphery where they likely encounter an environment rich in CD47-expressing cells (such as CAFs). This engages SIRPα on the myeloid cells, skewing them towards a suppressive phenotype and inhibiting their potential to phagocytose tumour cell-derived material. As a result, this could limit their capacity to present antigen and/or express critical anti-tumorigenic cytokines. The cells in turn acquire a suppressive phenotype that impairs T

cell reactivity to the tumour. Blocking this interaction on M-MDSCs and moDCs may increase tumour cell clearance and reduce expression of T cell suppressive molecules.

CD47-SIRPα signalling induces changes in cellular energetics.

We subsequently examined whether SIRPα-mediated inhibition of phagocytosis in myeloid cells induces a suppressive phenotype through altering the metabolic state of the MDSCs. Reactive oxygen species (ROS) production by tumour infiltrating immune cells has been correlated with more immunosuppressive phenotypes [28,60,61]. *In vitro* differentiated moDC and M-MDSC expressed intracellular ROS to equivalent levels in the presence or absence of tumour-derived factors (Figure 6A). Interestingly, rCD47 stimulation induced a small but significant increase in ROS generation by TCM-conditioned moDCs and M-MDSCs, and SIRPα blockade restored the level to baseline (Figure 6B). These data show that enhanced immunosuppression induced by CD47-SIRPα interaction is associated with an increased intracellular ROS. Importantly, TCM conditioning alone did not enhance ROS production and additional rCD47 stimulation was required. This led us to speculate that while tumour-derived factors are critical for regulating the immunosuppressive phenotype of moDCs and M-MDSCs, CD47 expressed by the TME may be needed to enhance a metabolic shift in the cells.

Considering the shift in ROS production alongside recent reports indicating that glycolysis might provide the energetic intermediates required for immune activation and antigen presentation[62,63], we then examined the effects of CD47-SIRPα on glycolysis. Indeed, phagocytosis mediated by engagement of CD47-SIRPα was accompanied by a small but significant decrease in glucose uptake (measured by NBDG uptake) for both moDC and M-MDSCs (Figure 6C) and was restored with SIRPα blockade (Figure 6C). Interestingly, rCD47 stimulation of moDCs and M-MDSCs induced an increase in surface expression of GLUT1, the main transporter responsible for glucose uptake, and this was further enhanced in the presence of SIRPα blockade (Figure 6D).

Further evidence suggests that tumour-infiltrating myeloid populations can modulate their activation state by increasing the synthesis and secretion of ATP where it is rapidly catabolized into adenosine[64,65]. Its accumulation in solid tumours then impairs anti-tumour T-cell responses[66]. We therefore looked further downstream to a general metabolic energetic marker, measuring the total ATP production as an indicator of the energetic state of cells. The more suppressive TCM-treated moDCs and M-MDSCs displayed a greater accumulation of ATP compared with GM-CSF treated cells in line with reports of impaired immunity (Figure 6E and 6F). Additionally, stimulation with CD47 induced a further, significant accumulation of intracellular ATP which was effectively abrogated by anti-SIRPα treatment in both GM-CSF and TCM treated conditions (Figure 6F).

Together, these data indicate that CD47-SIRPα engagement reduced the energetic requirements of moDCs and M-MDSCs, and this was associated with acquisition of a more suppressive phenotype. This shift in metabolic state was reversed upon SIRPα blockade.

Anti-SIRPα therapy restores antigen uptake, processing and presentation in tumours.

We next sought to determine whether disrupting the CD47-SIRPα interaction in moDCs and M-MDSCs and the accompanying changes in cell phenotype translated to an activation of pro-inflammatory functions, restoration of phagocytosis and antigen uptake, processing and presentation. Using the *in vitro* culture system, we identified that in addition to enhanced uptake of cellular debris after SIRPα blockade (Figure 5), antigen processing was also enhanced. All myeloid subsets tested could proteolytically cleave the modified version of Ovalbumin, DQ-OVA, with cDC2s and moDCs being more efficient than M-MDSCs (Figure 7A and Supplementary Figure 4A and B). However, the proportion of moDCs, M-MDSCs and cDC2s processing DQ-OVA significantly increased after SIRPα blockade, only in the presence of rCD47 (Figure 7A and Supplementary Figure 4A and B). The levels of processing within moDCs and M-MDSCs, and to a lesser extent cDC2s also increased (Figure 7B and Supplementary Figure 4C). This shows that antigen processing, both in terms of the number of cells processing and the amount of antigen processed by individual myeloid cells after rCD47 ligation was enhanced by anti-SIRPα treatment.

Having shown the effects of SIRPα blockade on the antigen sampling and processing capacity *in vitro*, we then examined the effects of SIRPα blockade on these functions within tumours *in vivo*. Following anti-SIRPα treatment of B16.F10.GFP tumour-bearing mice (melanoma cells overexpressing GFP; Supplementary Figure 4D), we detected a significant increase in the frequency of moDCs, M-MDSCs and cDC2s sampling tumour-derived material as determined by detection of tumour-derived GFP signal within the cells (Figure 7C and Supplementary Figure 4E). The amount of tumour-cell debris engulfed by myeloid cells also increased upon SIRPα blockade (Figure 7D), actively showing that SIRPα blockade enhances both the number of tumour-associated myeloid cells sampling material and the phagocytic capacity of individual cells *in vivo*. Lastly, in B16.F10 tumours which overexpressed cytoplasmic OVA, SIRPα blockade resulted in increased presentation of the OVA antigenic peptide SIINFEKL complexed with MHCI on the surface of moDCs, M-MDSCs and cDC2s (Figure 7E and 7F). These data suggest that blocking SIRPα restores the ability of moDCs and M-MDSCs to phagocytose dead or dying tumour cells *in vivo* then proteolytically process and present tumour antigen to infiltrating T cells.

Blockade of SIRPα signalling alters the immune landscape and slows the growth of established tumours.

Since SIRPα blockade reverts MDSCs to a less suppressive phenotype, promotes phagocytosis, antigen processing and presentation of tumour derived material (Figure 7C-7F), we then tested the impact of SIRPα blockade, and its affects, on B16.F10 tumour development. Mice bearing palpable tumours received anti-SIRPα antibody or IgG control at days 5 and 8 post-tumour induction (when moDCs and M-MDSCs dominate the myeloid infiltrate). Blockade of SIRPα significantly impaired the growth of established tumours by day 11 post-tumour induction compared with isotype control treated mice

(Figure 8A). Importantly, within each experiment we tested the bioavailability of SIRPα after treatment with the blocking antibody. Here, loss of detectable SIRPα signal confirmed that the blocking antibody treatment had penetrated the tumour-tissue and was occupying SIRPα epitopes on myeloid cells (Figure 8B).

The suppression of tumour growth with SIRPα blockade was accompanied by a remodelling of the immune microenvironment. A significant increase in $MHCII^+$ M-MDSCs was detected, suggesting that these cells had become more mature upon treatment (Figure 8C). This correlated with an increase in CD8 T cell abundance, which when compared to Treg infiltration that was unchanged upon treatment, resulted in an increased CD8:Treg ratio, typical of improved prognosis (Figure 8D)[67]. Increased cytotoxic T cell infiltration in the presence of myeloid cells with enhanced antigen presentation capability (Figure 7E-F) likely contributed to the impairment of tumour growth. Further examination of myeloid composition showed that there was a decrease in the proportion of moDCs and G-MDSCs in treated mice compared to control (Figure 8E). While no difference in M-MDSCs recruitment was observed (Figure 8E), we observed a slight increase in the relative proportion of M-MDSCs expressing CX3CR1 and a significant increase in CX3CR1 expression (Supplementary Figure 5B and 5C). This coincided with an increase in cDC1s, thus shifting the tumour back towards a phenotype reminiscent of that observed in the early day 5 lesions (Figure 1A and Supplementary Figure 5A). These data suggest that in addition to a restoration of myeloid cell phagocytic potential along with enhanced antigen processing and presentation capabilities, SIRPα blockade partially restores M-MDSC maturation and reduces the recruitment of suppressive myeloid cell subtypes into the tumour.

Lastly, to determine if this was a melanoma specific myeloid response, we treated mice bearing syngeneic pancreatic[68] or breast tumours[69] (that express similar or higher levels of CD47 compared to B16.F10 cells, Supplementary Figure 5D) using the same treatment regimen. As observed in melanoma, blockade of SIRPα supported a significant slowing of tumour growth in both tumour models (Figure 8F and 8G). Together these data indicate that disruption of the CD47-SIRPα signalling axis modulates myeloid composition and functionality towards a pro-inflammatory state. These cells are more capable of uptake, processing and presentation of tumour-derived material to infiltrating T cells, which in the absence of suppressive mediators, exert cytotoxic activity against the tumour and supports resolution.

Discussion

While immunotherapies have changed the landscape of cancer therapy, many patients fail to mount a long-term response to current therapies and in many cases experience toxicities due to overt T cell activation[9,70]. Therefore, targeting molecules that modulate phagocytosis and antigen presentation by myeloid cells alone or in combination with T

cell immune checkpoint therapy may mitigate some of these toxicities. This dual targeting approach would likely support an effective anti-tumour immune response.

Here we have shown how SIRPα expressing myeloid cells encounter a CD47 rich microenvironment as they infiltrate the tumour. As T cells and CAFs, the main source of CD47 in the melanoma model, are predominantly located at the tumour edge along the boundary with healthy tissue, it is likely that engagement of CD47 by myeloid cells occurs as the cells first enter the tumour before they penetrate the core. Engagement of SIRPα with CD47 on myeloid cells [36,38,57], contributes to the generation of an immune suppressive environment by reducing sampling, processing and presentation of tumour-derived antigen to infiltrating T cells. Furthermore, it augments expression of molecules involved in mediating T cell suppression, namely FASL, PD-L1 and IDO. Disruption of this pathway induced significant changes in recruitment and activity of multiple myeloid populations, tipping the balance from suppression towards inflammation, and was sufficient to slow tumour growth by increasing tumour cell phagocytosis and a subsequent increase in cytotoxic T cell infiltration.

To date, the majority of work to target phagocytosis has focused on disruption of CD47-SIRPα through the blockade of CD47, with numerous phase 1-2 clinical trials underway in haematological malignancies and solid tumours[21,50,71,72]. However, this may prove problematic as many normal cells also express CD47, including red blood cells and platelets, and as such significant off target toxicities have been reported. Thus SIRPα, and its more restricted expression offers an attractive alternative target, with potentially lower toxicity[40,44,73]. Indeed, we showed that even in an aggressive tumour, SIRPα blockade dampened the inhibitory signal which contributed to the myeloid cells suppressive state and induced higher T $CD8^+$:T_{reg} ratio within the TME. Consistent with work from Matozaki and colleagues, who showed that treatment of renal tumours with a high affinity anti-SIRPα antibody reduced tumour volume and increased CD8 T cell infiltration[74] and macrophages[75], we showed a similar phenomenon (using a different antibody clone) in a single syngeneic murine model of melanoma, pancreatic adenocarcinoma and breast adenocarcinoma. This shows that modulation of myeloid cell phagocytosis is a key regulator of anti-tumour immunity that is dysregulated in multiple tumour types, however this has only been interrogated in a single mouse model per tumour type. Furthermore, CD47-SIRPα interactions increased the suppressive capacity of myeloid populations *in vitro*, but its disruption with a SIRPα neutralising antibody shifted the cells to a more proinflammatory state. There was a concomitant reduction in expression of key immunosuppressive molecules and a reversion of the inhibition of T cell proliferation induced by a CD47 rich TME.

Our data indicate that modulation of the suppressive myeloid state, may at least be in part driven by changes to the phagocytosis pathway, and capacity to present antigen. Indeed, when myeloid cells encountered a CD47 rich environment, impaired phagocytosis of tumour cell debris was observed. Treatment with the SIRPα neutralising antibody boosted sampling of material, particularly by M-MDSCs, as well as enhanced antigen

processing and cross-presentation on MHCI. Changes in functional state were further supported by an altered glucose uptake and redistribution of cellular ATP. Less phagocytosis and cellular processing seen with CD47-mediated acquisition of a more suppressive phenotype was reflected in reduced energetic requirements and ATP accumulation. Hammami et al. previously demonstrated that bone marrow derived MDSCs increased ATP and NADPH production during maturation, indicating deterioration of metabolic activity, and development of an immunosuppressive state[76]. Accordingly, we observed that CD47 was contributing, in part, to establishing an immunosuppressive state which was reversed upon anti-SIRPα treatment and reactivation of more pro-inflammatory function. These findings are consistent with recent work by Baumann et al. who reported that metabolism and energetic state correlated with MDSC mediated T cell suppression through passage and accumulation of toxic metabolites within the cells [77]. Consequently, rather than modulating accumulation of myeloid cells to impact tumour clearance, SIRPα blockade instead favours myeloid reprogramming to drive activation and tumoricidal function of other infiltrating populations, such as CD8 T cells and cDC1s.

This work contributes to the growing body of evidence showing that combining SIRPα blockade as an innate checkpoint inhibitor with anti-PD1 or CTLA4 which targets T cell exhaustion, may improve therapeutic efficacy by boosting antigen uptake and presentation to enhanced numbers of reawakened T cells.

Limitations of the study

We show here that disruption of CD47-SIRPα axis through inhibition of SIRPα on myeloid cells supports a restoration of phagocytosis, antigen processing and presentation capacity, a more mature and activated immune phenotype and is accompanied by altered energetic profiles. However, there are several limitations to our study. It is not known if these metabolic adaptations are integral to the SIRPα signalling axis and are required for effector rather than suppressive functions. Further investigation would be required to thoroughly assess how cellular energetics influences MDSC function. Although an increased infiltration of CD8 T cells was detected within anti-SIRPα-treated tumours, we did not evaluate their activation status or localisation within tumours. Both would provide valuable information linking their presence with therapeutic impairment of tumour growth and for assessing efficacy of combination therapies with immune checkpoint blockade on T cell responses. Whilst we implemented both cellular and peptide-based approaches to investigate functional outputs of CD47-SIRPα signalling, there remains a possibility that different sources of CD47 stand to differentially impact myeloid cell behaviour. In addition, the efficacy of SIRPα on myeloid cell function was analysed in only one murine model for each disease modality. Testing SIRPα blockade in additional murine models, particularly genetically engineered tumour models, would further support our findings.

Authors contributions

J.D.S and H.M. supervised the study, assisted with analysis and co-wrote the manuscript, C.Z performed experiments and analysed the data, W.M. performed experiments and provided skin datasets, and S.E.D. performed bioinformatics analysis and critically reviewed the manuscript.

Acknowledgements

The authors would like to thank staff at the MRC ARES animal facility for assistance with *in vivo* experiments, members of the CIMR flow cytometry core for assistance with flow cytometry applications, and Professor David Tuveson (Cold Spring Harbor Laboratories) for the murine pancreatic cancer cell line used in syngeneic models. This work was supported by Medical Research Council Core funding.

Declaration of interests

The authors declare no competing interests.

ST*R METHODS

RESOURCE AVAILABILITY

Lead contact

Further information and requests for resources and reagents should be directed to and will be fulfilled by the Lead Contact Jacqueline D. Shields (jacqueline.shields@nottingham.ac.uk)

Materials availability

Key resources including details of key reagents and cell lines used are available in the Key Resources table. Any unique reagents generated in this study are available from the Lead Contact with a completed Materials Transfer Agreement. Datasets are listed in the key resources table.

Data and Code availability

- This paper analyses existing, publicly available data. The accession numbers for which are listed in Methods and key resources table.
- This paper does not report original code.
- Any additional information can be obtained from the lead contact upon request.

EXPERIMENTAL MODEL AND SUBJECT DETAILS

Mice

Wild-type C57BL/6 mice were obtained from the in-house breeding core within the MRC ARES facility. Adult female mice aged between 8 to 12 weeks of age were used for experiments. Animals were socially housed in individually ventilated cages with enrichment. All experiments were performed after review and approval by MRC Laboratory of Molecular Biology Animal and Ethical Review Board (AWERB) and approved by the Home Office in accordance with the Animals (Scientific Procedures) Act 1986 and ARRIVE guidelines. Non-invasive tumour measurements and intraperitoneal (I.P.) drug injections were performed by trained animal technicians at ARES, who, where possible, were blinded to experimental groups.

METHODS DETAILS

B16.F10 murine melanoma model

B16.F10, B16.F10 overexpressing ovalbumin (OVA) or B16.F10-GFP cells were passaged following standard protocol and re-suspended at a density of $2.5x10^5$ in 50µL of sterile saline for injection. Cells were injected subcutaneously into the right shoulder. Mice were sacrificed 5-, 9- or 11-days post tumour induction by exposure to carbon dioxide, followed by cervical dislocation or exsanguination by cardiac puncture (when blood samples were required). For anti-SIRPα treatment, mice received 125µg of Ultra-LEAF™ Purified anti-mouse CD172a (SIRPα; 144037, Biolegend) Antibody or a rat IgG1 isotype control (400427, Biolegend) by intraperitoneal injection. The first dose was administered once tumours reached 3mm in size (normally at Day 5 post-tumour induction) followed by a second dose on Day 8 post-tumour induction. Three days later, mice were sacrificed and the tumours and blood were harvested for analysis. To measure phagocytosis *in vivo*, mice were inoculated with $2.5x10^5$ B16.F10-GFP cells and treated with or without anti-SIRPα as described above. For assays measuring the antigen presentation capacity of MDSCs, mice received $4x10^5$ B16.F10-OVA cells and were treated with anti-SIRPα as above. However, for these experiments, mice were sacrificed on Day 9 rather than Day 11 post-tumour induction for analysis. For pancreatic cancer syngeneic tumours, $1x10^6$ mM1 pancreatic cancer cells, derived from a murine model of pancreatic adenocarcinoma generated on a C57BL/6 background (kindly gifted by Professor Dave Tuveson, CSHL), were injected subcutaneously into the flank of C57BL/6 mice and treated as above, sacrificing on Day 11 post-tumour induction. For orthotopic breast tumours, we injected E0771 cells (CH3 BIOSYSTEMS) at a density of $2.5x10^5$ in 50µL into the mammary fat pad of C57BL/6 mice. Mice were treated with anti-SIRPα on days 10 and 13 and were sacrificed on day 16.

Processing of tumour and blood

Resected tumours were mechanically dissociated using a blade and digested in 1mg/ml collagenase D (Roche), 1mg/ml collagenase A (Roche) and 0.4mg/ml DNase (Roche) in PBS, at 37^{o}C for 45min before collagenase activity was neutralized with 5mM EDTA. Digested tumours were then passed through 70µm cell strainers (Falcon) and washed. Single cells suspensions were pelleted at 300g for 5min, resuspended in PBS and seeded into a round-bottomed 96-well plates (Corning). Blood samples obtained from cardiac puncture were collected in K_2EDTA tubes; Samples were incubated in 5mL of red blood cell lysis buffer (RBC Lysis Buffer; 150mM NH4Cl, 1mM KHCO3, 0.1mM EDTA in dH2O) at room temperature (RT) for 5min and then washed with 10X PBS. All samples were then stained for flow cytometry.

Generation of tumour conditioned media

For tumour cell conditioned medium (TCM), B16.F10 cells were grown until 60-70% confluent in Dulbecco's Modified Eagle Medium (DMEM, Life Technologies) containing 10% Foetal Bovine Serum (FBS) and 1% penicillin/streptomycin (P/S). Medium was collected 24h later and centrifuged at 600g for 10min to remove cellular debris. Media was collected, snap frozen and stored at -80 °c.

Isolation of murine cells from bone marrow and spleen

Femurs and tibias were flushed from C57BL/6 mice with PBS. Cells were resuspended to obtain a single cell suspension free of bone debris. After washing, RBCs were lysed. For cell isolation from the spleen, the spleen was removed from C57BL/6 mice and disrupted using a 25-gauge needle and then passed through a 70µm strainer using a 1ml syringe plunger, before RBCs were lysed as described above.

***In vitro* differentiation of HSCs into MDSCs**

HSCs were isolated from bone marrow using Magnetic-activated cell sorting (MACS – as described below) and half of the cells were resuspended in RPMI, supplemented with 20ng/mL GM-CSF (Peprotech, Cat: 315-03) and the other half was resuspended in a 1:1 mix of TCM and RPMI, supplemented with 20ng/mL GM-CSF. Cells were seeded at a density of 2.5x10^{5} cells and matured for 5 days with media changes performed daily. The MDSC were subsequently harvested by gentle pipetting and isolated as described below.

Magnetic-activated cell sorting to isolate immune populations

Sca-1^{+} HSCs were isolated from bone marrow-derived cell suspensions in MACS Buffer (0.5% v/v Bovine Serum Albumin [BSA] and 2mM EDTA in PBS) as per manufactures guidelines. For T cell isolation from spleen, cells were incubated with the Pan T cell Isolation Kit II (Miltenyi Biotec, 130-095-130) according to manufacturer's instructions. Columns were then washed with MACS buffer and unlabelled CD3^{+} T cells were collected in the flow through.

For isolation of MDSCs and moDCs after *in vitro* differentiation from HSCs, cells were gently resuspended and collected to limit the presence of highly differentiated adherent cells. M-MDSCs and moDCs expressing CD11b and Ly6C were harvested using two different MACs kits, one to isolate CD11b+ cells (Miltenyi Biotec Cat: 130-113-233) and subsequently $Ly6C^+$ cells (Miltenyi Biotec Cat: 130-111-776) as per the manufacturer's instructions. For isolation of $CD11b^+Ly6C^+$ cells from *in vivo* tumours, tumour tissue was processed until a single-cell suspension was obtained as described above, and MACS sorted in the same manner as *in vitro* cultures. In all cases, flow cytometry was performed to confirm the purity of MACS sorted HSCs, moDCs and M-MDSCs. Viable cells were counted using a hemacytometer and re-suspended at the desired concentration for *in vitro* assays.

In vitro CD47 active protein treatment on myeloid cell phenotype and function

The recombinant mouse CD47 protein (Active) (cat: ab231160) was reconstituted to 5µg/ml in PBS. Then, 50ul of solution was used to coat the wells of a 96 well, non-pyrogenic polystyrene flat or round (for T cell proliferation assay) bottom plate. Plates were sealed with parafilm and kept overnight at 4°C to allow even coating. Plates were then washed with PBS. After HSC differentiation *in vitro* in the presence of GM-CSF or GM-CSF supplemented with TCM, differentiated MDSCs were added to the plate and incubated for 2 days at 37°C and 5% CO_2. Cells were then washed and analysed by flow cytometry.

SIRPα blockade on myeloid cell phenotype and function

The Ultra-LEAF™ Purified anti-mouse CD172a (SIRPα) Antibody (Cat: 144037) was prepared in the appropriate media and incubated with myeloid cells on ice for 30min prior to incubation in wells coated with active CD47. The antibody was used at the concentration of 115nM for treatment of tumours *in vivo* and used at 1nM or titrated 1:10 from 200nM for assays measuring the phagocytic capacity of the *in vitro* differentiated cells.

Cell labelling

For experiments assessing T cell proliferation, T cells harvested from spleen were stained with Cell-Trace CFSE as previously described (Thermo, Cat: C34554). For experiments assessing the phagocytic capacity of *in vitro* differentiated MDSCs, B16.F10 and CAFs cells were stained with Cell-Trace Far red as per the manufacturer's instructions (Thermo, Cat: C345664). Cells were re-suspended at a density of 0.5–10 x 10^6 cells/ml in 1 mL of media. 5mM CFSE or Cell-Trace Far red, was added and cells were gently mixed and incubated for 7min, at RT. Cells were washed and resuspended in IMDM + 5% FCS + 0.5ul of β-mercaptoethanol (Sigma, Cat: M7522) for T cells, or RPMI + 10% FCS + P/S for B16.F10 and CAFs, for 20min at 37°C and 5% CO_2 to allow the cells to recover.

T cell proliferation assay

96 well flat-bottomed plates were coated with 2.5µg/mL LEAF™ anti-mouse CD3e antibody (Biolegend, Clone: 145-2C11, Cat:14-0031) and incubated for 2h at 37°C. Excess antibody was washed off. CFSE-stained T cells were re-suspended in IMDM + 5% FCS + 0.5ul of β-mercaptoethanol (Sigma, Cat: M7522) + P/S supplemented with 1µg/mL of soluble anti-CD28 antibody (Biolegend, Clone 37.51, Cat: 16-0281) and seeded on the coated 96 well plate at a density of 2 x 10^5 T cells per well. T cells were stimulated for 24h at 37°C and 5% CO_2. T cells were then harvested and co-cultured with MDSCs isolated from tumours or differentiated from HSCs *in vitro* at a ratio of 1:4 myeloid cells:T cells. Co-cultures were incubated at 37°C and 5% CO_2 for 48h with media replenishments performed after 24h. Samples were then prepared for flow cytometry analysis.

Detection of reactive oxygen species (ROS)

Ly6C$^+$ cells were isolated from *in vitro* moDC and M-MDSC cultures and plated at 6x10^4 cells per well in a 96 nonpyrogenic flat bottom plate where some wells were coated with active CD47 protein. In certain conditions, cells were pre-treated with anti-SIRPα blocking antibody as described above. The cells were incubated for 4h in GM-CSF alone, GM-CSF-TCM, GM-CSF-TCM-activeCD47 or anti-SIRPα-GM-CSF-TCM-activeCD47. After incubation, cells were washed and treated with 10µM 2′,7′-Dichlorodihydrofluorescein diacetate (DCFDA; Sigma-Aldrich) in basal DMEM for 25min. Immediately after, cells were washed twice with PBS and transferred to ice. Then, they were resuspended in PBS with Live/Dead Fixable Violet (Thermo, Cat: 62248) viability dye, diluted 1:1000, for 3min, to label dead cells. Samples were Immediately washed once with PBS and run on an LSR Fortessa cell analyzer (BD, Biosciences) to measure DCFDA levels as a readout for intracellular ROS.

Detection of metabolites in moDCs and M-MDSCs

For measurements of glucose uptake and GLUT-1 expression, we depleted glucose in myeloid cells for 4h and then treated with 200µM of a fluorescently-labeled deoxyglucose analog (2-NBDG; Invitrogen, cat: N13195) for another 20min at 37°C and 5% CO_2. In the meantime, the GLUT1 (Novus Biologicals, Cat: NB110-39113) antibody was preincubated with an Alexa-fluor-647 chicken anti-rabbit APC (used at 35nM; Life technology, Cat: A21443). Immediately after, cells were washed and rapidly stained with the GLUT1 antibody complex at 4^{o}C and analysed by flow cytometry. For ATP detection, cells were analysed using an ATP detection kit (Merck, Cat: 119107), according to the manufacturer's protocol. To measure NADH, a hexokinase colorimetric assay was used. The activity of hexokinase in cellular lysates was analysed by measuring the NADH production over time, according to the manufacturer's protocol (Sigma–Aldrich, Cat: MAK037).

Phagocytosis assays

To generate CD47-expressing cell debris for phagocytosis assays, B16.F10 (expressing little CD47) cells and CAFs (expressing high levels of CD47) were stained using Cell Trace Far red (Thermo, Cat: C345664) and resuspended to a concentration of $3x10^7$ cells/ml in a 1:1 mix of TCM and RPMI + 10% FCS + P/S media supplemented with 20ng/mL GM-CSF (Peprotech, Cat: 315-03). Half of the labelled cells were killed to generate cell debris by heat induction in a thermomixer for 5 minutes at 98°C. The dead cell debris was chilled in ice and mixed again with the remaining live cells.

Different myeloid populations obtained from differentiated HSCs were seeded at $5x10^4$ cells per well in a 96 nonpyrogenic flat bottom well plate and kept overnight in a 1:1 mix of TCM and RPMI + 10% FCS + P/S supplemented with 20ng/mL GM-CSF (Peprotech, Cat: 315-03). After treating with anti-SIRPα blocking antibody, cells were added to CD47 coated plates. Then, 50µl cell suspension containing $7.5x10^4$ live and $7.5x10^4$ dead labelled CD47 high or low cells was added to the wells containing the different myeloid populations and incubated for 4h at 37°C and 5% CO_2. Subsequently, co-cultures were washed with PBS, put on ice to block further phagocytosis and stained for flow cytometry to detect the degree of phagocytosis by the myeloid cells based on Cell Trace Far Red levels detected in the myeloid cells.

OVA processing

Myeloid cells exposed to control media, SIRPα blockade and/or CD47 coating were pulsed with DQ-Ovalbumin (Cat: D-12053, Thermo) at 100µg/ml for 10min at 37°C and then washed 3 times with ice cold PBS containing 5% FBS. Then, the media was exchanged and samples were incubated for a further 35min. Cells were then washed and transferred to ice for flow cytometry staining.

Flow cytometry staining

Samples were resuspended in PBS with Live/Dead Fixable Violet (Thermo, Cat: 62248) viability dye, diluted 1:1000, for 15min. After washing, samples were incubated with fluorophore-conjugated primary antibodies prepared at 1:300 dilution in FACS buffer (0.5% BSA in PBS) and mixed 1:1 with Fc block (generated in house from a rat 2.4G2 hybridoma cell line)), for 40min, at 4°C. After surface staining, and if intracellular epitope detection was required, samples were fixed, permeabilised and stained in accordance with the FoxP3/ Transcription Factor Staining Kit (eBioscience, Cat: 00- 5523). Briefly, cells were incubated with fluorophore-conjugated primary antibodies, diluted 1:300 in permeabilization buffer, for 30min at RT. After washing, samples were run on an LSR Fortessa cell analyzer (BD Biosciences) and analysed using FlowJo version 10. (FlowJo, BD Biosciences).

Immunofluorescence staining

10µm frozen tissue sections were air dried and fixed in a 1:1 mix of acetone and methanol, for 2min at -20°C. Next, sections were washed in PBS for 10min before incubation in blocking solution containing 10% chicken or donkey serum and 2% BSA for 1h, at RT. The sections were then placed in a humidified chamber and incubated with unconjugated primary antibodies against SIRPα (1:50, P84 Biolegend), CD11b (1:100, biotin conjugated M1/70 eBiosciences) and fluorescently conjugated Ly6C (1:50, AL-21 Biolegend) diluted in blocking buffer, overnight at 4°C. Following 3 x 5min washes in PBST (PBS with 0.1% Tween), sections were incubated with 1:300 Chicken anti-Rat Conjugated AF594 (A21471; for SIRPα) and Streptavidin conjugated AF 647 (S32357; for CD11b, both from Life Technologies) for 1h, at RT. Sections were then counterstained with 1µg/ml of 4',6-diamidino-2-phenylindole (DAPI, Thermo, D1306), for 10min, and mounted onto 22 x 50 mm glass coverslips with SlowFade Gold Antifade Mountant (Life Technologies; Cat: S36936). Sections were imaged on a Zeiss 880 laser scanning confocal microscope using a 40x oil objective (ZEISS).

Analysis of public datasets

To evaluate expression of CD47 and SIRPα patterns within the murine melanoma microenvironment, single cell data from Davidson et al.[58] was accessed online from http://www.teichlab.org/data/. The raw sequencing data is also available from ArrayExpress: E-MTAB-7427 (deposited by authors).

QUANTIFICATION AND STATISTICAL ANALYSIS

To evaluate statistical significance between two samples a t-test was performed. For multiple comparisons, one way or two-way ANOVA were employed with a Dunnett, Šidák or Tukey post- hoc test depending on the pairwise comparisons being performed. Data are expressed as mean ± SEM, where a different cell isolate and batch of TCM was used for each experiment and was therefore considered a different biological sample. Data were analysed using Graphpad Prism 9 Software packages.

References

1 Borghaei, H. *et al.* Nivolumab versus Docetaxel in Advanced Nonsquamous Non-Small-Cell Lung Cancer. *N Engl J Med* **373**, 1627-1639 (2015). https://doi.org:10.1056/NEJMoa1507643

2 Hirano, F. *et al.* Blockade of B7-H1 and PD-1 by monoclonal antibodies potentiates cancer therapeutic immunity. *Cancer Res* **65**, 1089-1096 (2005).

3 Leach, D. R., Krummel, M. F. & Allison, J. P. Enhancement of antitumor immunity by CTLA-4 blockade. *Science* **271**, 1734-1736 (1996). https://doi.org:10.1126/science.271.5256.1734

4 Mehra, R. *et al.* Efficacy and safety of pembrolizumab in recurrent/metastatic head and neck squamous cell carcinoma: pooled analyses after long-term follow-up in KEYNOTE-012. *Br J Cancer* **119**, 153-159 (2018). https://doi.org:10.1038/s41416-018-0131-9

5 Motzer, R. J. *et al.* Nivolumab versus everolimus in patients with advanced renal cell carcinoma: Updated results with long-term follow-up of the randomized, open-label, phase 3 CheckMate 025 trial. *Cancer* **126**, 4156-4167 (2020). https://doi.org:10.1002/cncr.33033

6 Rosenberg, J. E. *et al.* Atezolizumab in patients with locally advanced and metastatic urothelial carcinoma who have progressed following treatment with platinum-based chemotherapy: a single-arm, multicentre, phase 2 trial. *Lancet* **387**, 1909-1920 (2016). https://doi.org:10.1016/S0140-6736(16)00561-4

7 Smyth, M. J., Ngiow, S. F., Ribas, A. & Teng, M. W. L. Combination cancer immunotherapies tailored to the tumour microenvironment. *Nat. Rev. Clin. Oncol.* **13**, 143--158 (2016).

8 Bai, R. *et al.* Mechanisms of Cancer Resistance to Immunotherapy. *Front Oncol* **10**, 1290 (2020). https://doi.org:10.3389/fonc.2020.01290

9 Sharma, P., Hu-Lieskovan, S., Wargo, J. A. & Ribas, A. Primary, Adaptive, and Acquired Resistance to Cancer Immunotherapy. *Cell* **168**, 707-723 (2017). https://doi.org:10.1016/j.cell.2017.01.017

10 Binnewies, M. *et al.* Understanding the tumor immune microenvironment (TIME) for effective therapy. *Nat Med* **24**, 541-550 (2018). https://doi.org:10.1038/s41591-018-0014-x

11 Jones, J. O., Moody, W. M. & Shields, J. D. Microenvironmental modulation of the developing tumour: an immune-stromal dialogue. *Mol Oncol* (2020). https://doi.org:10.1002/1878-0261.12773

12 Broz, M. L. *et al.* Dissecting the tumor myeloid compartment reveals rare activating antigen-presenting cells critical for T cell immunity. *Cancer Cell* **26**, 638-652 (2014). https://doi.org:10.1016/j.ccell.2014.09.007

13 Cui, S., Reichner, J. S., Mateo, R. B. & Albina, J. E. Activated murine macrophages induce apoptosis in tumor cells through nitric oxide-dependent or -independent mechanisms. *Cancer Res* **54**, 2462-2467 (1994).

14 Katoh, H. *et al.* CXCR2-expressing myeloid-derived suppressor cells are essential to promote colitis-associated tumorigenesis. *Cancer Cell* **24**, 631-644 (2013). https://doi.org:10.1016/j.ccr.2013.10.009

15 Kuang, D. M. *et al.* Activated monocytes in peritumoral stroma of hepatocellular carcinoma foster immune privilege and disease progression through PD-L1. *J Exp Med* **206**, 1327-1337 (2009). https://doi.org:10.1084/jem.20082173

16 Ong, S. M. *et al.* Macrophages in human colorectal cancer are pro-inflammatory and prime T cells towards an anti-tumour type-1 inflammatory response. *Eur J Immunol* **42**, 89-100 (2012). https://doi.org:10.1002/eji.201141825

17 Ratnam, N. M. *et al.* NF-kappaB regulates GDF-15 to suppress macrophage surveillance during early tumor development. *J Clin Invest* **127**, 3796-3809 (2017). https://doi.org:10.1172/JCI91561

18 Al Sayed, M. F. *et al.* T-cell-Secreted TNFalpha Induces Emergency Myelopoiesis and Myeloid-Derived Suppressor Cell Differentiation in Cancer. *Cancer Res* **79**, 346-359 (2019). https://doi.org:10.1158/0008-5472.CAN-17-3026

19 Glass, C. K. & Natoli, G. Molecular control of activation and priming in macrophages. *Nat Immunol* **17**, 26-33 (2016). https://doi.org:10.1038/ni.3306

20 Allavena, P. *et al.* IL-10 prevents the differentiation of monocytes to dendritic cells but promotes their maturation to macrophages. *Eur J Immunol* **28**, 359-369 (1998). https://doi.org:10.1002/(SICI)1521-4141(199801)28:01<359::AID-IMMU359>3.0.CO;2-4

21 Cheng, P. *et al.* Inhibition of dendritic cell differentiation and accumulation of myeloid-derived suppressor cells in cancer is regulated by S100A9 protein. *J Exp Med* **205**, 2235-2249 (2008). https://doi.org:10.1084/jem.20080132

22 Obermajer, N. & Kalinski, P. Key role of the positive feedback between PGE(2) and COX2 in the biology of myeloid-derived suppressor cells. *Oncoimmunology* **1**, 762-764 (2012). https://doi.org:10.4161/onci.19681

23 Nefedova, Y. *et al.* Hyperactivation of STAT3 is involved in abnormal differentiation of dendritic cells in cancer. *J Immunol* **172**, 464-474 (2004). https://doi.org:10.4049/jimmunol.172.1.464

24 Jiang, M. *et al.* Interleukin-6 Trans-Signaling Pathway Promotes Immunosuppressive Myeloid-Derived Suppressor Cells via Suppression of Suppressor of Cytokine Signaling 3 in Breast Cancer. *Front Immunol* **8**, 1840 (2017). https://doi.org:10.3389/fimmu.2017.01840

25 Veglia, F., Sanseviero, E. & Gabrilovich, D. I. Myeloid-derived suppressor cells in the era of increasing myeloid cell diversity. *Nat Rev Immunol* **21**, 485-498 (2021). https://doi.org:10.1038/s41577-020-00490-y

26 Delano, M. J. *et al.* MyD88-dependent expansion of an immature GR-1(+)CD11b(+) population induces T cell suppression and Th2 polarization in sepsis. *J Exp Med* **204**, 1463-1474 (2007). https://doi.org:10.1084/jem.20062602

27 Alshetaiwi, H. *et al.* Defining the emergence of myeloid-derived suppressor cells in breast cancer using single-cell transcriptomics. *Sci Immunol* **5** (2020). https://doi.org:10.1126/sciimmunol.aay6017

28 Nagaraj, S. *et al.* Altered recognition of antigen is a mechanism of CD8+ T cell tolerance in cancer. *Nat Med* **13**, 828-835 (2007). https://doi.org:10.1038/nm1609

29 Wculek, S. K. *et al.* Dendritic cells in cancer immunology and immunotherapy. *Nat Rev Immunol* **20**, 7-24 (2020). https://doi.org:10.1038/s41577-019-0210-z

30 Cancel, J. C., Crozat, K., Dalod, M. & Mattiuz, R. Are Conventional Type 1 Dendritic Cells Critical for Protective Antitumor Immunity and How? *Front Immunol* **10**, 9 (2019). https://doi.org:10.3389/fimmu.2019.00009

31 Binnewies, M. *et al.* Unleashing Type-2 Dendritic Cells to Drive Protective Antitumor CD4(+) T Cell Immunity. *Cell* **177**, 556-571 e516 (2019). https://doi.org:10.1016/j.cell.2019.02.005

32 Verhasselt, V. *et al.* Induction of FOXP3-expressing regulatory CD4pos T cells by human mature autologous dendritic cells. *Eur J Immunol* **34**, 762-772 (2004). https://doi.org:10.1002/eji.200324552

33 Banerjee, D. K., Dhodapkar, M. V., Matayeva, E., Steinman, R. M. & Dhodapkar, K. M. Expansion of FOXP3high regulatory T cells by human dendritic cells (DCs) in vitro and after injection of cytokine-matured DCs in myeloma patients. *Blood* **108**, 2655-2661 (2006). https://doi.org:10.1182/blood-2006-03-011353

34 Majeti, R. *et al.* CD47 is an adverse prognostic factor and therapeutic antibody target on human acute myeloid leukemia stem cells. *Cell* **138**, 286-299 (2009). https://doi.org:10.1016/j.cell.2009.05.045

35 Willingham, S. B. *et al.* The CD47-signal regulatory protein alpha (SIRPa) interaction is a therapeutic target for human solid tumors. *Proc Natl Acad Sci U S A* **109**, 6662-6667 (2012). https://doi.org:10.1073/pnas.1121623109

36 Matozaki, T., Murata, Y., Okazawa, H. & Ohnishi, H. Functions and molecular mechanisms of the CD47-SIRPalpha signalling pathway. *Trends Cell Biol* **19**, 72-80 (2009). https://doi.org:10.1016/j.tcb.2008.12.001

37 Zhao, H. *et al.* CD47 Promotes Tumor Invasion and Metastasis in Non-small Cell Lung Cancer. *Sci Rep* **6**, 29719 (2016). https://doi.org:10.1038/srep29719

38 Tsai, R. K. & Discher, D. E. Inhibition of "self" engulfment through deactivation of myosin-II at the phagocytic synapse between human cells. *J Cell Biol* **180**, 989-1003 (2008). https://doi.org:10.1083/jcb.200708043

39 Oldenborg, P. A. CD47: A Cell Surface Glycoprotein Which Regulates Multiple Functions of Hematopoietic Cells in Health and Disease. *ISRN Hematol* **2013**, 614619 (2013). https://doi.org:10.1155/2013/614619

40 Zhao, X. W. *et al.* CD47-signal regulatory protein-alpha (SIRPalpha) interactions form a barrier for antibody-mediated tumor cell destruction. *Proc Natl Acad Sci U S A* **108**, 18342-18347 (2011). https://doi.org:10.1073/pnas.1106550108

41 Liu, Y. *et al.* Signal regulatory protein (SIRPalpha), a cellular ligand for CD47, regulates neutrophil transmigration. *J Biol Chem* **277**, 10028-10036 (2002). https://doi.org:10.1074/jbc.M109720200

42 Gholamin, S. *et al.* Disrupting the CD47-SIRPalpha anti-phagocytic axis by a humanized anti-CD47 antibody is an efficacious treatment for malignant pediatric

brain tumors. *Sci Transl Med* **9** (2017). https://doi.org:10.1126/scitranslmed.aaf2968

43 Liu, X. *et al.* CD47 blockade triggers T cell-mediated destruction of immunogenic tumors. *Nat Med* **21**, 1209-1215 (2015). https://doi.org:10.1038/nm.3931

44 Murata, Y., Saito, Y., Kotani, T. & Matozaki, T. CD47-signal regulatory protein alpha signaling system and its application to cancer immunotherapy. *Cancer Sci* **109**, 2349-2357 (2018). https://doi.org:10.1111/cas.13663

45 Andrechak, J. C., Dooling, L. J. & Discher, D. E. The macrophage checkpoint CD47 : SIRPalpha for recognition of 'self' cells: from clinical trials of blocking antibodies to mechanobiological fundamentals. *Philos Trans R Soc Lond B Biol Sci* **374**, 20180217 (2019). https://doi.org:10.1098/rstb.2018.0217

46 Zhang, W. *et al.* Advances in Anti-Tumor Treatments Targeting the CD47/SIRPalpha Axis. *Front Immunol* **11**, 18 (2020). https://doi.org:10.3389/fimmu.2020.00018

47 Tseng, D. *et al.* Anti-CD47 antibody-mediated phagocytosis of cancer by macrophages primes an effective antitumor T-cell response. *Proc Natl Acad Sci U S A* **110**, 11103-11108 (2013). https://doi.org:10.1073/pnas.1305569110

48 Weiskopf, K. *et al.* CD47-blocking immunotherapies stimulate macrophage-mediated destruction of small-cell lung cancer. *J Clin Invest* **126**, 2610-2620 (2016). https://doi.org:10.1172/JCI81603

49 Logtenberg, M. E. W. *et al.* Glutaminyl cyclase is an enzymatic modifier of the CD47- SIRPalpha axis and a target for cancer immunotherapy. *Nat Med* **25**, 612-619 (2019). https://doi.org:10.1038/s41591-019-0356-z

50 Advani, R. *et al.* CD47 Blockade by Hu5F9-G4 and Rituximab in Non-Hodgkin's Lymphoma. *N Engl J Med* **379**, 1711-1721 (2018). https://doi.org:10.1056/NEJMoa1807315

51 Brierley, C. K. *et al.* The effects of monoclonal anti-CD47 on RBCs, compatibility testing, and transfusion requirements in refractory acute myeloid leukemia. *Transfusion* **59**, 2248-2254 (2019). https://doi.org:10.1111/trf.15397

52 Chao, M. P. *et al.* Calreticulin is the dominant pro-phagocytic signal on multiple human cancers and is counterbalanced by CD47. *Sci Transl Med* **2**, 63ra94 (2010). https://doi.org:10.1126/scitranslmed.3001375

53 Gauttier, V. *et al.* Selective SIRPalpha blockade reverses tumor T cell exclusion and overcomes cancer immunotherapy resistance. *J Clin Invest* **130**, 6109-6123 (2020). https://doi.org:10.1172/JCI135528

54 Kuo, T. C. *et al.* Targeting the myeloid checkpoint receptor SIRPalpha potentiates innate and adaptive immune responses to promote anti-tumor activity. *J Hematol Oncol* **13**, 160 (2020). https://doi.org:10.1186/s13045-020-00989-w

55 Zhou, Z. *et al.* Tumor-intrinsic SIRPA promotes sensitivity to checkpoint inhibition immunotherapy in melanoma. *Cancer Cell* **40**, 1324-1340 e1328 (2022). https://doi.org:10.1016/j.ccell.2022.10.012

56 Barry, S. T., Gabrilovich, D. I., Sansom, O. J., Campbell, A. D. & Morton, J. P. Therapeutic targeting of tumour myeloid cells. *Nat Rev Cancer* **23**, 216-237 (2023). https://doi.org:10.1038/s41568-022-00546-2

57 Abe, T. *et al.* Signal regulatory protein alpha blockade potentiates tumoricidal effects of macrophages on gastroenterological neoplastic cells in syngeneic immunocompetent mice. *Ann Gastroenterol Surg* **2**, 451-462 (2018). https://doi.org:10.1002/ags3.12205

58 Davidson, S. *et al.* Single-Cell RNA Sequencing Reveals a Dynamic Stromal Niche That Supports Tumor Growth. *Cell Rep* **31**, 107628 (2020). https://doi.org:10.1016/j.celrep.2020.107628

59 Bouguermouh, S. *et al.* CD47 expression on T cell is a self-control negative regulator of type 1 immune response. *J Immunol* **180**, 8073-8082 (2008). https://doi.org:10.4049/jimmunol.180.12.8073

60 Schmielau, J. & Finn, O. J. Activated granulocytes and granulocyte-derived hydrogen peroxide are the underlying mechanism of suppression of t-cell function in advanced cancer patients. *Cancer Res* **61**, 4756-4760 (2001).

61 Lu, T. *et al.* Tumor-infiltrating myeloid cells induce tumor cell resistance to cytotoxic T cells in mice. *J Clin Invest* **121**, 4015-4029 (2011). https://doi.org:10.1172/JCI45862

62 Ganeshan, K. & Chawla, A. Metabolic regulation of immune responses. *Annu Rev Immunol* **32**, 609-634 (2014). https://doi.org:10.1146/annurev-immunol-032713-120236

63 Xu, Y. *et al.* Glycolysis in Innate Immune Cells Contributes to Autoimmunity. *Front Immunol* **13**, 920029 (2022). https://doi.org:10.3389/fimmu.2022.920029

64 Cekic, C., Day, Y. J., Sag, D. & Linden, J. Myeloid expression of adenosine A2A receptor suppresses T and NK cell responses in the solid tumor microenvironment. *Cancer Res* **74**, 7250-7259 (2014). https://doi.org:10.1158/0008-5472.CAN-13-3583

65 Cohen, H. B. *et al.* TLR stimulation initiates a CD39-based autoregulatory mechanism that limits macrophage inflammatory responses. *Blood* **122**, 1935-1945 (2013). https://doi.org:10.1182/blood-2013-04-496216

66 Jin, D. *et al.* CD73 on tumor cells impairs antitumor T-cell responses: a novel mechanism of tumor-induced immune suppression. *Cancer Res* **70**, 2245-2255 (2010). https://doi.org:10.1158/0008-5472.CAN-09-3109

67 Goda, N. *et al.* The ratio of CD8 + lymphocytes to tumor-infiltrating suppressive FOXP3 + effector regulatory T cells is associated with treatment response in invasive breast cancer. *Discov Oncol* **13**, 27 (2022). https://doi.org:10.1007/s12672-022-00482-5

68 Cioffi, M. *et al.* Inhibition of CD47 Effectively Targets Pancreatic Cancer Stem Cells via Dual Mechanisms. *Clin Cancer Res* **21**, 2325-2337 (2015). https://doi.org:10.1158/1078-0432.CCR-14-1399

69 Yuan, J. *et al.* High expression of CD47 in triple negative breast cancer is associated with epithelial-mesenchymal transition and poor prognosis. *Oncol Lett* **18**, 3249-3255 (2019). https://doi.org:10.3892/ol.2019.10618

70 Conroy, M. & Naidoo, J. Immune-related adverse events and the balancing act of immunotherapy. *Nat Commun* **13**, 392 (2022). https://doi.org:10.1038/s41467-022-27960-2

71 Yang, H., Xun, Y. & You, H. The landscape overview of CD47-based immunotherapy for hematological malignancies. *Biomark Res* **11**, 15 (2023). https://doi.org:10.1186/s40364-023-00456-x

72 Jiang, Z., Sun, H., Yu, J., Tian, W. & Song, Y. Targeting CD47 for cancer immunotherapy. *J Hematol Oncol* **14**, 180 (2021). https://doi.org:10.1186/s13045-021-01197-w

73 Adams, S. *et al.* Signal-regulatory protein is selectively expressed by myeloid and neuronal cells. *J Immunol* **161**, 1853-1859 (1998).

74 Yanagita, T. *et al.* Anti-SIRPalpha antibodies as a potential new tool for cancer immunotherapy. *JCI Insight* **2**, e89140 (2017). https://doi.org:10.1172/jci.insight.89140

75 Sakamoto, M. *et al.* Anticancer efficacy of monotherapy with antibodies to SIRPalpha/SIRPbeta1 mediated by induction of antitumorigenic macrophages. *Proc Natl Acad Sci U S A* **119** (2022). https://doi.org:10.1073/pnas.2109923118

76 Hammami, I. *et al.* Immunosuppressive activity enhances central carbon metabolism and bioenergetics in myeloid-derived suppressor cells in vitro models. *BMC Cell Biol* **13**, 18 (2012). https://doi.org:10.1186/1471-2121-13-18

77 Baumann, T. *et al.* Regulatory myeloid cells paralyze T cells through cell-cell transfer of the metabolite methylglyoxal. *Nat Immunol* **21**, 555-566 (2020). https://doi.org:10.1038/s41590-020-0666-9

Figure legends:

Figure 1. The myeloid compartment in B16.F10 melanoma shifts towards suppressive phenotypes as tumours develop. (A) Flow cytometry quantification of the percentage of DCs (CD11c+) and phagocytes (CD11b+CD11c-) within $CD45^+$ cells. **(B)** Flow cytometry quantification of MDSCs populations (moDCs; $CD11b^+CD11c^+Ly6C^+$, M-MDSCs; $CD11b^+CD11c^-Ly6C^+$ and G-MDSCs; $CD11b^+CD11c^-Ly6G^+$) within $CD45^+$ cells. **(C)** Flow cytometry quantification of the expression levels of immune modulatory markers PD-L1, FasL, ARG1 and NOS2 by moDCs, M-MDSCs and G-MDSCs. **(D)** Representative CFSE plots for CD8 T cell proliferation after culture alone, co-culture with tumour-derived

CD11b^{+}Ly6C^{-} cells or co-culture with a mix of tumour-derived moDCs and M-MDSCs. Black bar highlights the gated proliferated cells. **(E)** Flow cytometry quantification of the percentage of proliferating CD8 and CD4 cells cultured alone, co-cultured with tumour-derived CD11b^{+}Ly6C^{-} cells or a mix of moDCs and M-MDSCs. **(F)** Representative CFSE plots for CD4 and CD8 T cell proliferation after co-culture with pre-sorted, tumour-derived moDCs or M-MDSCs. Black bar highlights the gated proliferated cells. **(G)** Quantification of T cell suppression following incubation with pre-sorted, tumour-derived moDCs and M-MDSCs compared to T cells cultured alone. Data are mean ± SEM; ** = $p < 0.01$, *** = $p < 0.001$, **** = $p<0.0001$ using (A-C) Mixed effect analysis with a Tukey's post hoc test. (E and G) One-way ANOVA with a Tukey's post hoc test. (A-B) n=5 mice for day 5 and 9 tumours and n=6 for day 11 tumours, from two independent experiments comparing each cell type at day 5, 9 or 11 timepoints with the day 0 timepoint. (C) n=8 mice for day 5 tumours and n=6 mice for day 11 tumours from two independent experiments. (E) n=3 and (G) n=2 mice performed in duplicate from two different experiments.

Figure 2. Tumour conditioning of myeloid cells *in vitro* recapitulates the myeloid compartment shift towards suppressive phenotypes. Flow cytometry quantification of the differentiation of isolated SCA-1^{+} HSCs towards **(A)** cDCs and phagocytes and more specifically **(B)** moDCs, M-MDSC and G-MDSCs after treatment with either GM-CSF or GM-CSF supplemented TCM. **(C)** Representative CFSE plots for CD4 and CD8 T cell proliferation after incubation with *in vitro*-generated Ly6C^{+} myeloid cells in GM-CSF or GM-CSF supplemented TCM compared to T cells cultured alone. Black bar highlights the gated proliferated cells. **(D)** Quantification of the percentage of proliferating CD8 and CD4 cells cultured alone, co-cultured with GM-CSF or GM-CSF supplemented TCM differentiated mixed moDCs and M-MDSCs. **(E)** Flow cytometry quantification of expression of immune modulatory markers PD-L1, FasL, ARG1 and SIRPα by moDCs and M-MDSCs. Data are mean ± SEM; ** = $p < 0.01$, *** = $p < 0.001$, **** = $p<0.0001$. (A-B) Mixed effect analysis with a Tukey's post hoc test. (D) One-way ANOVA with a Tukey's post hoc test comparing each cell type at day 3 and 5 timepoints with the day 0 timepoint. (E) Two-way ANOVA with a Tukey's multiple comparisons post hoc test. (A-C) n=2 replicates for each condition from eight independent experiments. (D) n=7 and (E) n=3 independent experiments performed in triplicate.

Figure 3. Distribution of CD47 and SIRPα expression across the TME. (A) Clustering of stromal populations identified in B16.F10 melanomas and matched draining lymph nodes analysed from data previously published by Davidson et al[58], **(B)** Expression of CD47 and its cognate receptor, SIRPα, distributed across stromal clusters. **(C)** Violin plots highlighting widespread CD47 but restricted SIRPα expression across stromal subsets. **(D)** Flow cytometry quantification of CD47 expression at the protein level in T cells, (immunomodulatory) CAF 1, (myofibroblast) CAF 2, myeloid cells, endothelial cells (CD31+) and B16.F10 tumour cells. **(E)** Representative confocal image of a day 11 B16.F10 melanoma showing myeloid populations. Arrows indicate CD11b+Ly6C+SIRPα+ cells. Insets show zoom of selected ROI. Arrowheads depict cells

positive for CD11b but negative for Ly6C and SIRPα. DAPI (Grey), CD11b (red), Ly6C (green), SIRPα (Blue). Scale bar is 50μm. Data are mean ± SEM; * = $p < 0.05$, ** = $p < 0.01$, *** = $p < 0.001$, **** = $p<0.0001$. (D) One-way ANOVA with a Dunnett post hoc test. (D) n=3 replicates from two independent experiments.

Figure 4. CD47 stimulation promotes a suppressive phenotype in myeloid populations and is rescued by SIRPα blockade. (A) Flow cytometry quantification of expression levels of immune modulatory markers PD-L1, FasL, ARG1 and SIRPα by moDCs and M-MDSCs following stimulation with TCM or rCD47 (expressed as relative gMFI). **(B)** Flow cytometry quantification of the percentage of proliferating CD8 and CD4 cells measured by CFSE; cultured alone or co-cultured with a mixture of moDCs and M-MDSCs pre-treated with different combinations of TCM, rCD47 and anti-SIRPα. **(C)** Flow cytometry quantification of expression of PD-L1 and ARG1 by mixed moDC and M-MDSC cultures after treatment with TCM with or without rCD47 and anti-SIRPα. Data are mean ± SEM; * = $p < 0.05$, ** = $p < 0.01$, *** = $p < 0.001$, **** = $p<0.0001$. (A) Two-way ANOVA with a Tukey's multiple comparisons post hoc test. (B) Unpaired t-test. (C) One-way ANOVA with a Tukey's post hoc test. (A) three independent experiments each with n=3 replicates. (B) n=6 independent assays performed in triplicate. (C) n=6 independent assays for PD-L1 and n=3-4 independent assays for ARG1, each performed in triplicate.

Figure 5. Blockade of CD47-SIRPα interaction boosts the phagocytic capabilities of MDSCs. (A) Flow cytometry quantification of CD47 expression levels by B16.F10 melanoma, CAFs and dermal fibroblasts. **(B)** Schematic representation of the assay developed to measure the effects of CD47 on the phagocytic potential of different myeloid subsets. M-MDSCs and moDCs were mixed with a mix of fluorescently labelled CD47-high or -low expressing cells and their cell debris. Uptake of fluorescent debris by moDCs and M-MDSCs was then analysed by flow cytometry and quantified as the proportion of $CD45^+$ cells that are moDCs or M-MDSCs that have phagocytosed cell debris. **(C)** Flow cytometry quantification of uptake of labelled CD47-high or -low cell debris by moDCs and M-MDSCs. Quantification of phagocytosis by **(D)** moDCs and **(E)** M-MDSCs after co-culture with $CD47^{lo}$ or $CD47^{hi}$ cells in the presence or absence of SIRPα neutralising antibody. **(F)** Competition assay showing occupation of SIRPα epitopes by anti-SIRPα (P84) antibody. Upper panel: Quantification of gMFI signal detected for fluorophore conjugated anti-SIRPα antibody after epitope blockade by Ultra LEAF- SIRPα antibody. Lower panel: Quantification of gMFI signal detected for Ultra-LEAF antibody detected by fluorophore conjugated Rat IgG. Data are mean ± SEM; ** = $p < 0.01$, *** = $p < 0.001$, **** = $p<0.0001$. (A, C, D-E) One-way ANOVA with a Tukey's post hoc test. (A) n=1 performed in triplicate. (C, D-E) n=3 independent experiments performed in duplicate, (F) n=3 performed in triplicate.

Figure 6. CD47-SIRPα modulation enhances phagocytosis and modifies cellular energetics. (A) Flow cytometry quantification of intracellular DCFDA (ROS) signal detected in mixed moDCs and M-MDSCs grown in GM-CSF or GM-CSF supplemented TCM. **(B)** Representative flow cytometry histograms showing DCFDA signal in moDCs

and M-MDSCs in the presence of CD47 with (dark grey) or without (light grey) anti-SIRPα and quantification of DCFDA gMFI signal in each condition. **(C)** Quantification of uptake of the glucose analogue 2-NBDG *in vitro* by differentiated moDCs and M-MDSCs with or without CD47 stimulation in the presence or absence of anti-SIRPα. **(D)** Flow cytometry quantification of the glucose transporter GLUT-1 expression on the surface of *in vitro* differentiated moDCs and M-MDSCs with or without CD47 stimulation in the presence or absence of anti-SIRPα. **(E)** Quantification of intracellular ATP levels in mixed moDC and M-MDSC cultures grown in GM-CSF or GM-CSF supplemented TCM. **(F)** Quantification of intracellular ATP driven levels in mixed moDC and M-MDSC cultures grown in GM-CSF or GM-CSF supplemented TCM with or without CD47 stimulation in the presence or absence of anti-SIRPα. Data are mean ± SEM; * = $p < 0.05$, ** = $p < 0.01$, *** = $p < 0.001$, **** = $p<0.0001$. All data was normalised to the GM-CSF or untreated sample. (A, E) Paired t test. (B-D) One-way ANOVA with Dunnett's post hoc test. (F) One-way ANOVA with a Tukey's post hoc test. (A) Assays n=4 independent experiments each performed in triplicate. (B) n=3 independent experiments each performed in duplicate. (C-D) n=4 independent experiments each performed in triplicate. (E) n=4 independent experiments each performed in triplicate. (F) n=3 independent experiments each performed in triplicate.

Figure 7. SIRPα therapy induces phagocytosis, antigen processing and presentation in myeloid cells. (A) Flow cytometry quantification of the frequency of GM-CSF-supplemented-TCM treated moDCs and M-MDSCs that uptake and proteolytically process DQ-OVA antigen with or without CD47 stimulation, in the presence or absence of anti-SIRPα. **(B)** Quantification of the levels of DQ-OVA processed by moDCs and M-MDSCs (gMFI). Data normalised to GM-CSF-TCM condition. **(C)** Quantification of the abundance of moDCs, M-MDSCs and cDC2s that phagocytosed GFP^+ melanoma-derived material *in vivo* following therapeutic blockade of CD47-SIRPα signalling. Expressed as the proportion of $CD45^+$ cells that are moDCs or M-MDSCs that have phagocytosed GFP+ cell debris. **(D)** Quantification of the level of GFP material ingested by moDCs, M-MDSCs and cDC2s. For C-D, Data were normalised by the signal detected in the rat-IgG1 injected conditions. **(E)** Representative tSNE plots derived from the flow cytometry data (of total $CD45^+$ cells) showing that intratumoural $CD45^+Ly6C^+$ cells exhibit the highest level of SIINFEKL (OVA antigen) complexed with MHCI. **(F)** Quantification of presentation of the OVA peptide SIINFEKL by moDCs, M-MDSCs and cDC2s that was acquired by uptake and processing of material from B16.OVA melanoma cells. Data are mean ± SEM; * = $p < 0.05$, ** = $p < 0.01$. (A-B) One-way ANOVA with Tukey's multiple comparisons and Dunnett's post hoc test, respectively. (C-D and F) Two-way ANOVA with Tukey's multiple comparisons test. (A-B) n=3 performed in triplicate, (D and F) two independent experiments of n=4 mice each.

Figure 8. Therapeutic SIRPα blockade slows growth of established tumours in vivo. (A) Volume (mm^3) of B16.F10 melanomas grown in mice treated with rat-IgG1 (isotype control) or anti-SIRPα. **(B)** Representative flow cytometry histograms and quantification of expression levels showing SIRPα bioavailability at the tumour site in untreated, isotype

or anti-SIRPα treated mice. Only mice in which SIRPα signal was reduced were included in the analyses. **(C)** Flow cytometry quantification of MHCII expression by tumour infiltrating moDCs and M-MDSCs after treatment with anti-SIRPα or isotype. **(D)** Flow cytometry quantification of CD8+ T cells and Tregs (normalised to the percentage of CD45+ cells) and the ratio of CD8:Tregs. **(E)** Quantification of tumour infiltrating moDCs**,** M-MDSC and G-MDSCs (normalised to the percentage of CD45+ cells) after treatment with anti-SIRPα or isotype control. Data were normalised to the rat-IgG1 controls. **(E)** Volume (mm^3) of subcutaneously injected pancreatic ductal adenocarcinoma or orthotopic E0771 breast tumours treated with IgG or anti-SIRPα over 11 days. Data are mean ± SEM; * = $p < 0.05$, ** = $p < 0.01$, *** = $p < 0.001$, **** = $p<0.0001$. (A and D-G) Paired t-test. (B-C) One-way ANOVA with a Dunnett's post hoc test. (A-C and F-G) n=14 (rat-IgG1) and n=15 (anti-SIRPα-P84) from 5 independent experiments. (D) n=3 for each group from 3 independent experiments.

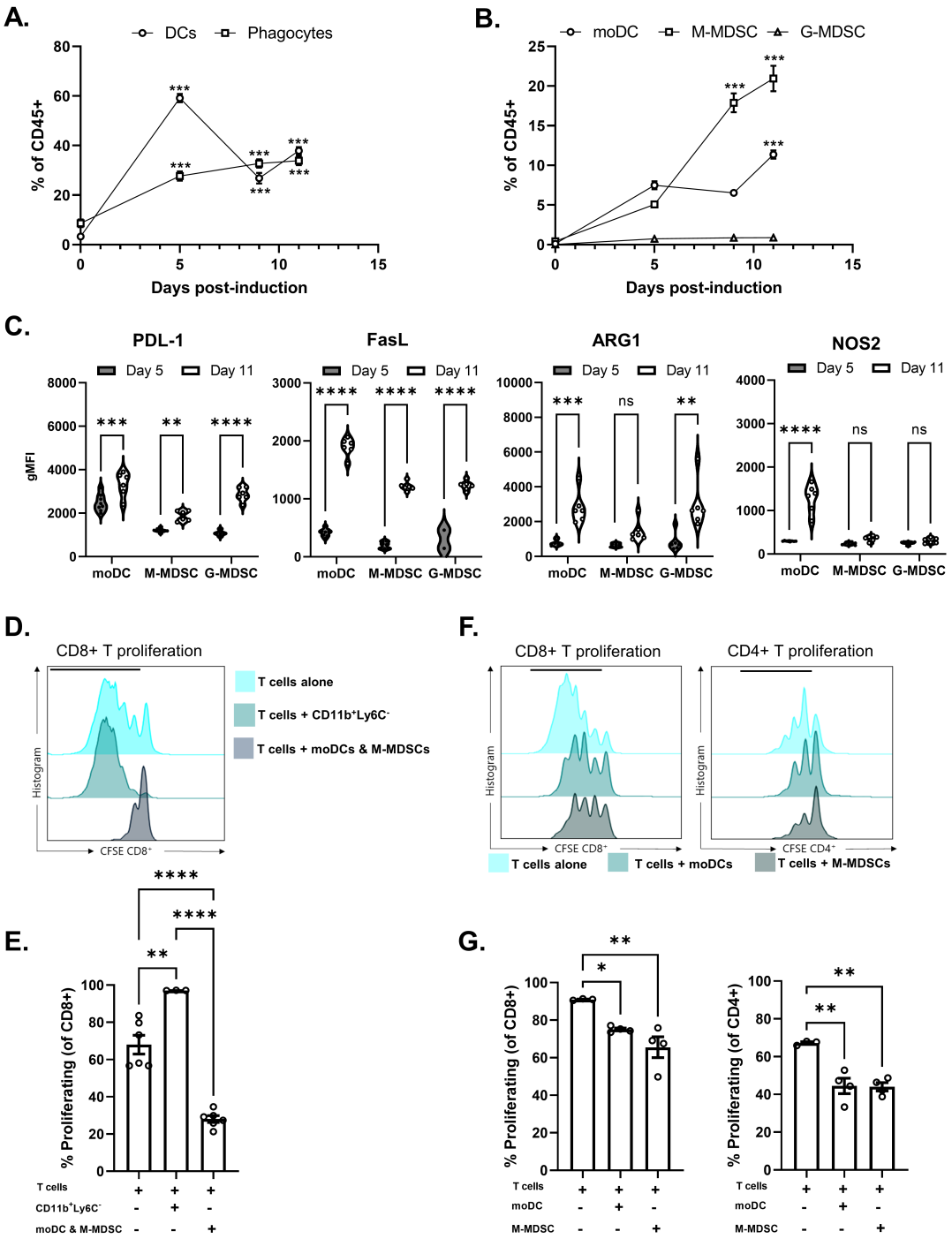
A.
DCs
Phagocytes
% of CD45+
Days post-induction
B.
moDC
M-MDSC
G-MDSC
% of CD45+
Days post-induction
C.
PDL-1
FasL
ARG1
NOS2
Day 5
Day 11
gMFI
moDC
M-MDSC
G-MDSC
ns
D.
CD8+ T proliferation
T cells alone
T cells + CD11b+Ly6C-
T cells + moDCs & M-MDSCs
Histogram
CFSE CD8+
F.
CD8+ T proliferation
CD4+ T proliferation
CFSE CD8+
CFSE CD4+
T cells alone
T cells + moDCs
T cells + M-MDSCs
E.
% Proliferating (of CD8+)
T cells
CD11b+Ly6C-
moDC & M-MDSC
G.
% Proliferating (of CD8+)
% Proliferating (of CD4+)
T cells
moDC
M-MDSC

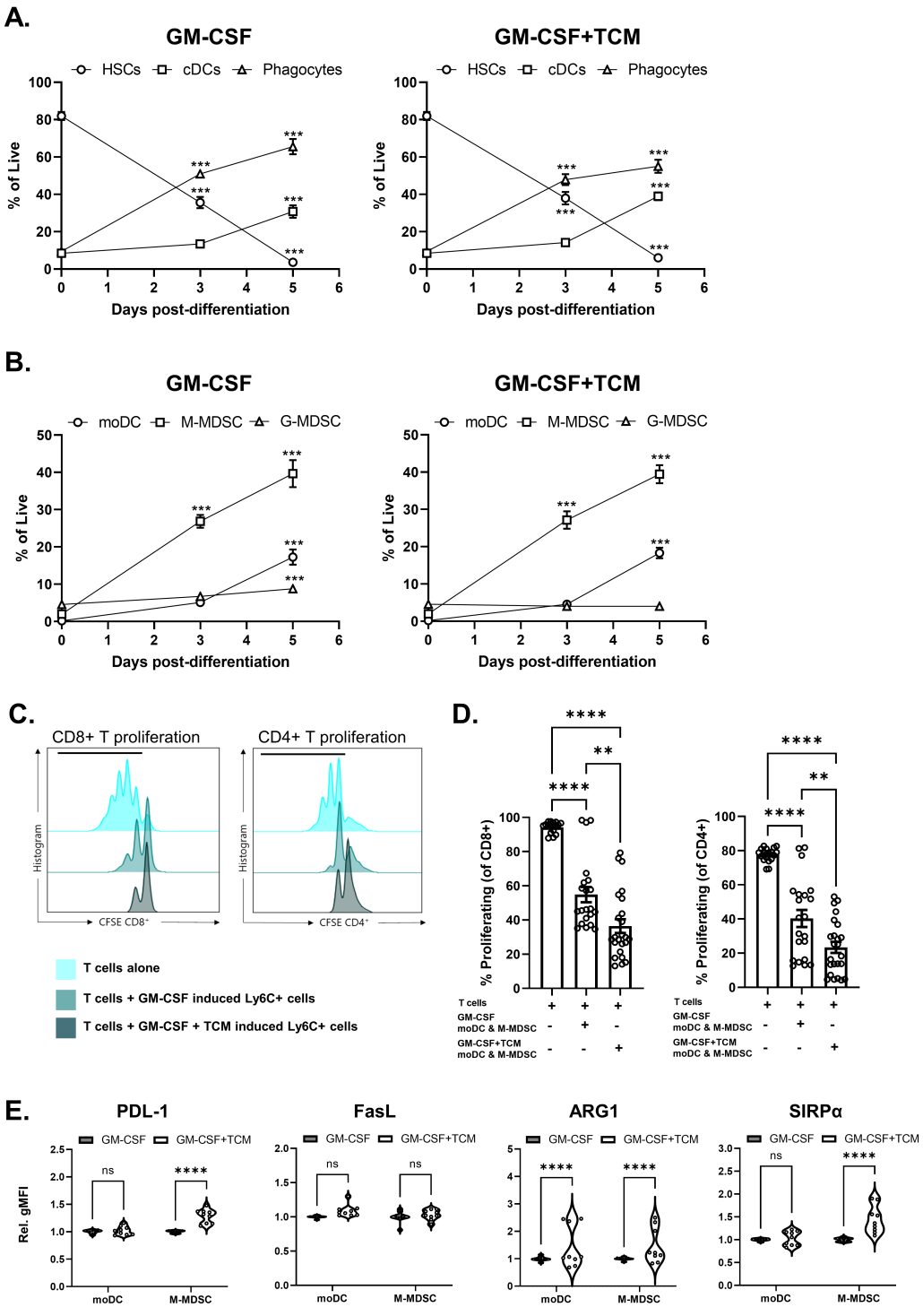
A.
GM-CSF
GM-CSF+TCM
HSCs
cDCs
Phagocytes
% of Live
Days post-differentiation
B.
moDC
M-MDSC
G-MDSC
C.
CD8+ T proliferation
CD4+ T proliferation
Histogram
CFSE CD8+
CFSE CD4+
T cells alone
T cells + GM-CSF induced Ly6C+ cells
T cells + GM-CSF + TCM induced Ly6C+ cells
D.
% Proliferating (of CD8+)
% Proliferating (of CD4+)
T cells
GM-CSF moDC & M-MDSC
GM-CSF+TCM moDC & M-MDSC
E.
PDL-1
FasL
ARG1
SIRPα
Rel. gMFI
GM-CSF
GM-CSF+TCM
moDC
M-MDSC
ns

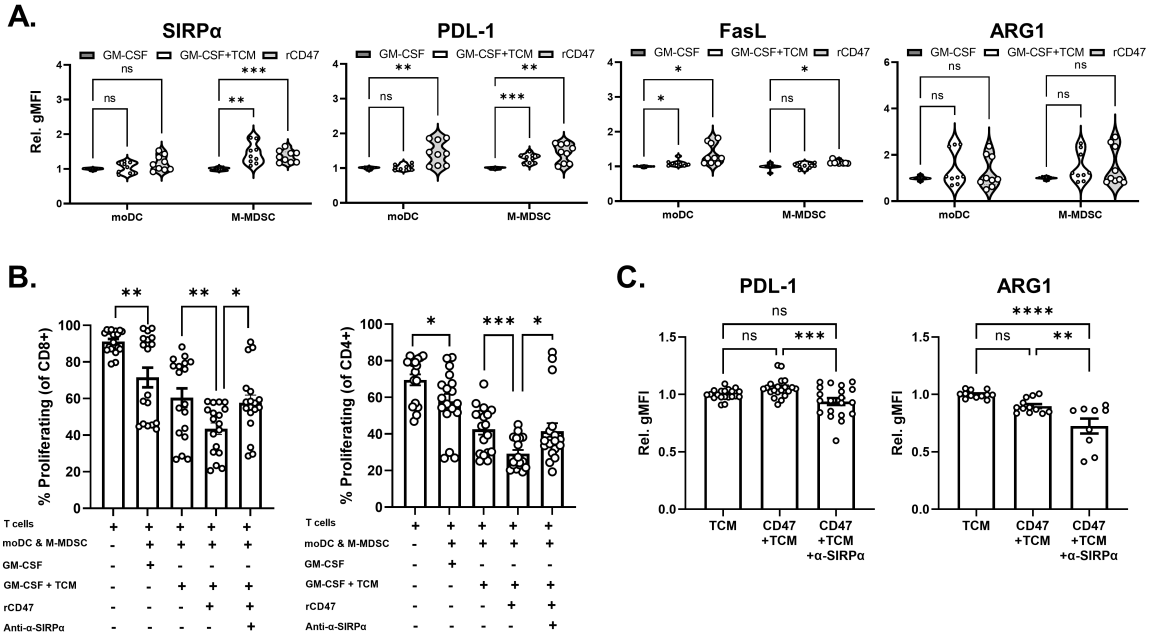
A.
SIRPα
PDL-1
FasL
ARG1
GM-CSF
GM-CSF+TCM
rCD47
Rel. gMFI
moDC
M-MDSC
B.
% Proliferating (of CD8+)
% Proliferating (of CD4+)
T cells
moDC & M-MDSC
GM-CSF
GM-CSF + TCM
rCD47
Anti-α-SIRPα
C.
PDL-1
ARG1
TCM
CD47 +TCM
CD47 +TCM +α-SIRPα

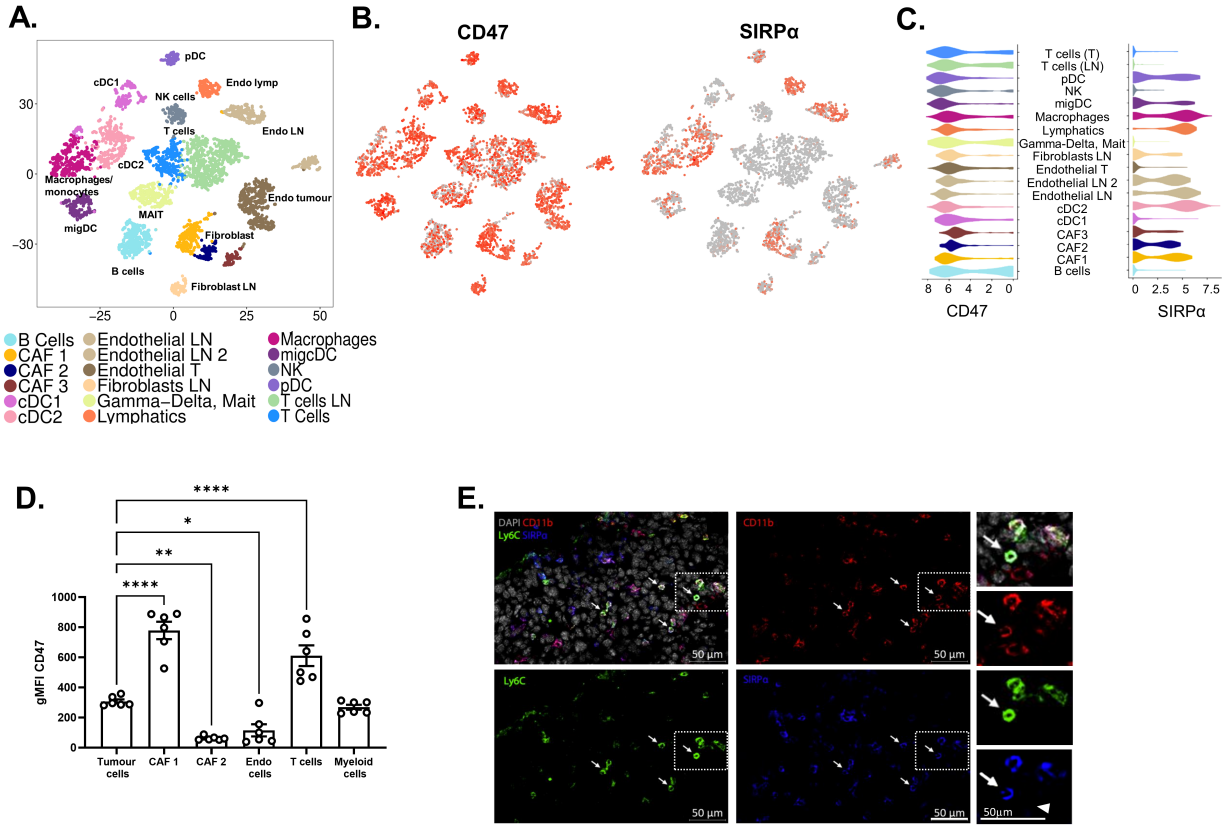
A.
pDC
cDC1
Endo lymp
NK cells
T cells
Endo LN
cDC2
Macrophages/ monocytes
Endo tumour
MAIT
migDC
Fibroblast
B cells
Fibroblast LN
B Cells
CAF 1
CAF 2
CAF 3
cDC1
cDC2
Endothelial LN
Endothelial LN 2
Endothelial T
Fibroblasts LN
Gamma–Delta, Mait
Lymphatics
Macrophages
migcDC
NK
pDC
T cells LN
T Cells
B.
CD47
SIRPα
C.
T cells (T)
T cells (LN)
pDC
NK
migDC
Macrophages
Lymphatics
Gamma-Delta, Mait
Fibroblasts LN
Endothelial T
Endothelial LN 2
Endothelial LN
cDC2
cDC1
CAF3
CAF2
CAF1
B cells
CD47
SIRPα
D.
gMFI CD47
Tumour cells
CAF 1
CAF 2
Endo cells
T cells
Myeloid cells
E.
DAPI CD11b Ly6C SIRPα
CD11b
Ly6C
SIRPα
50 µm

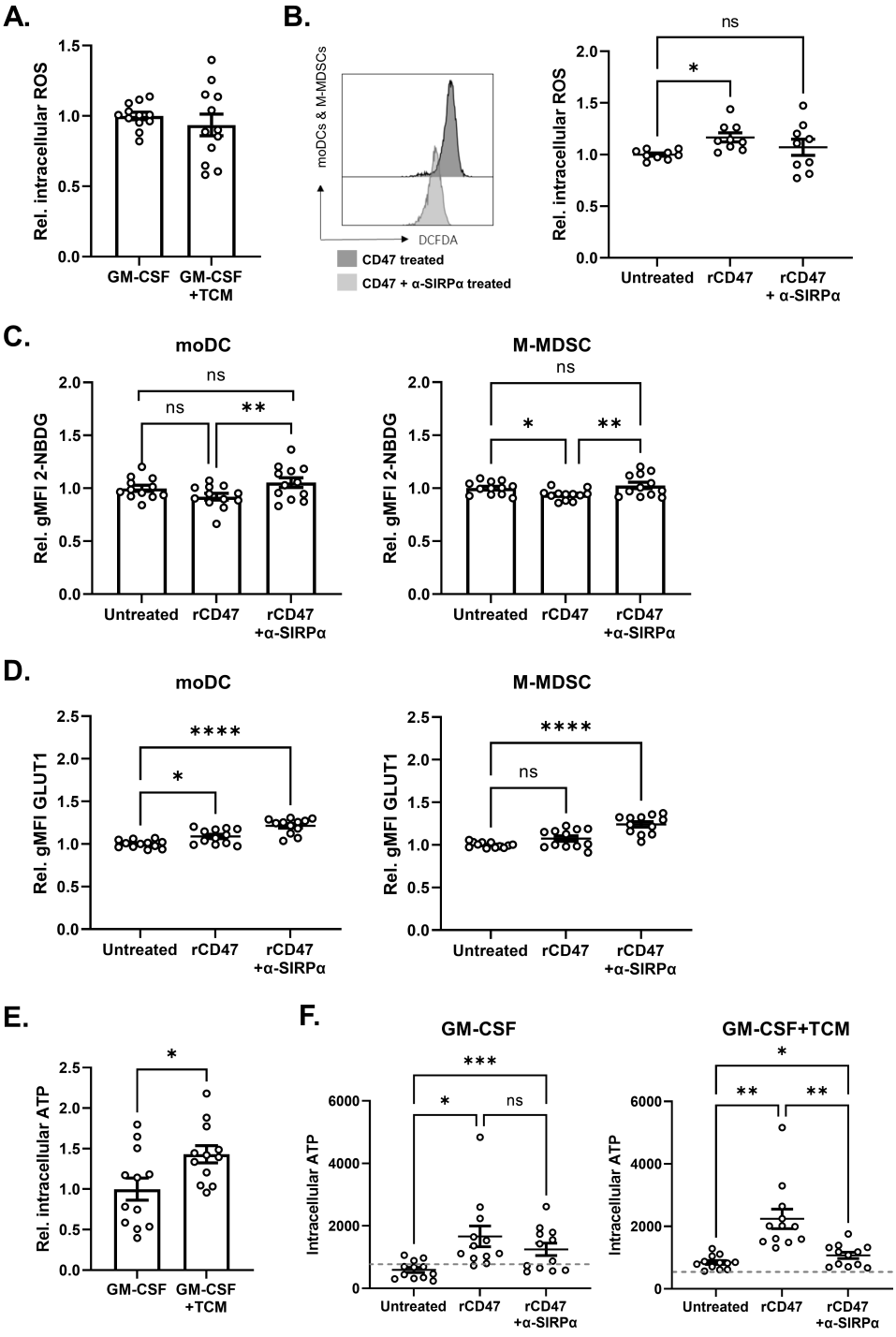
A.
Rel. intracellular ROS
GM-CSF
GM-CSF +TCM
B.
moDCs & M-MDSCs
DCFDA
CD47 treated
CD47 + α-SIRPα treated
Rel. intracellular ROS
Untreated
rCD47
rCD47 + α-SIRPα
C.
moDC
M-MDSC
Rel. gMFI 2-NBDG
D.
Rel. gMFI GLUT1
E.
Rel. intracellular ATP
F.
GM-CSF
GM-CSF+TCM
Intracellular ATP

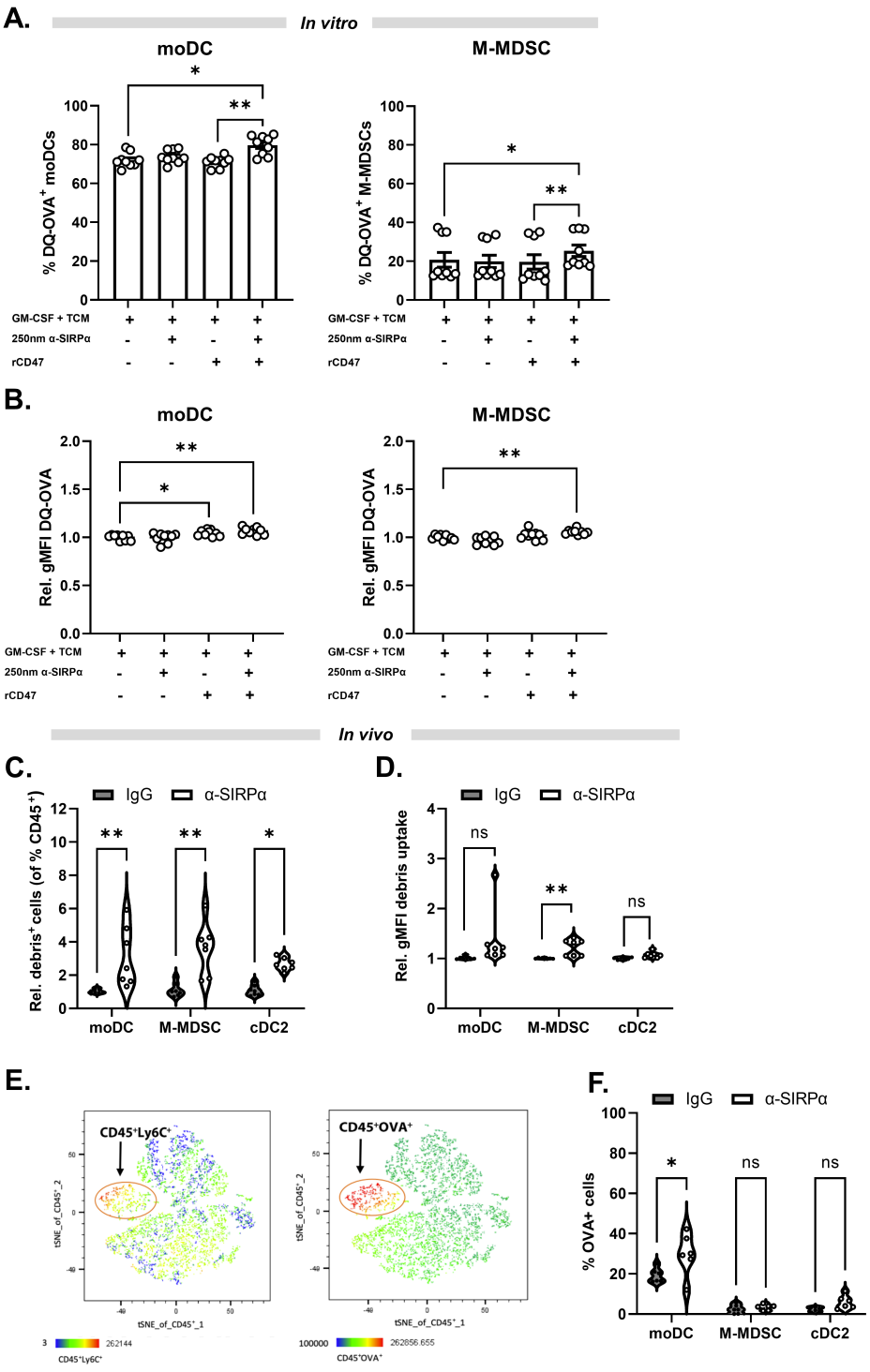
A.
In vitro
moDC
M-MDSC
% DQ-OVA+ moDCs
% DQ-OVA+ M-MDSCs
GM-CSF + TCM
250nm α-SIRPα
rCD47
B.
Rel. gMFI DQ-OVA
In vivo
C.
IgG
α-SIRPα
Rel. debris+ cells (of % CD45+)
D.
Rel. gMFI debris uptake
ns
E.
CD45+Ly6C+
CD45+OVA+
tSNE_of_CD45+_1
tSNE_of_CD45+_2
F.
% OVA+ cells

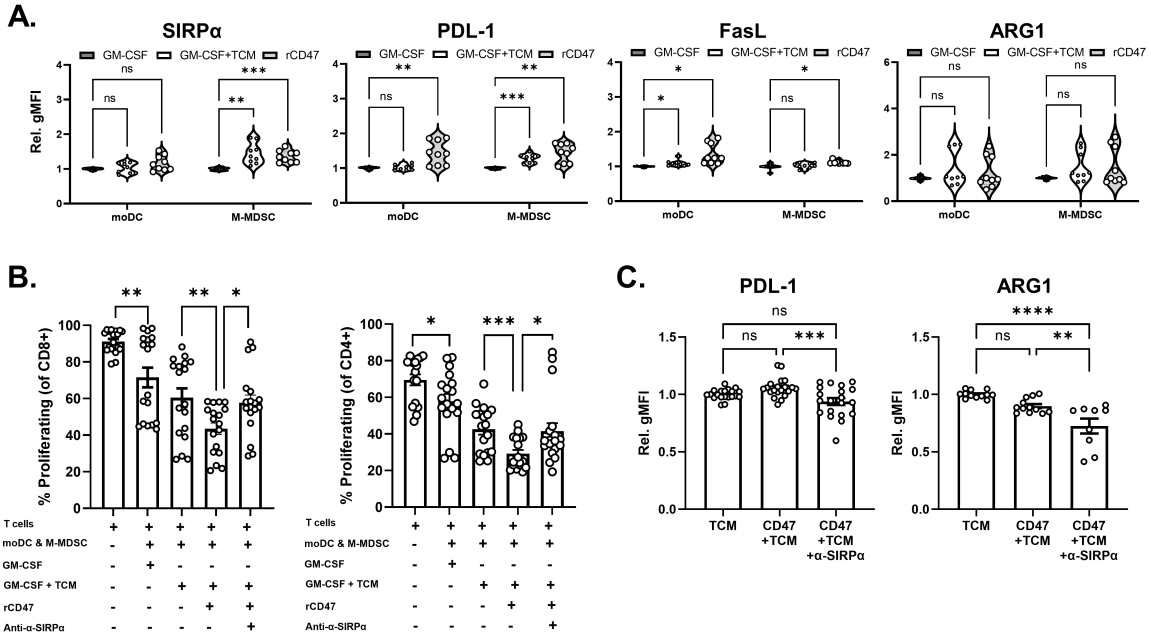
A.
SIRPα
PDL-1
FasL
ARG1
GM-CSF
GM-CSF+TCM
rCD47
Rel. gMFI
moDC
M-MDSC
ns
B.
% Proliferating (of CD8+)
% Proliferating (of CD4+)
T cells
moDC & M-MDSC
GM-CSF
GM-CSF + TCM
rCD47
Anti-α-SIRPα
C.
PDL-1
ARG1
TCM
CD47 +TCM
CD47 +TCM +α-SIRPα

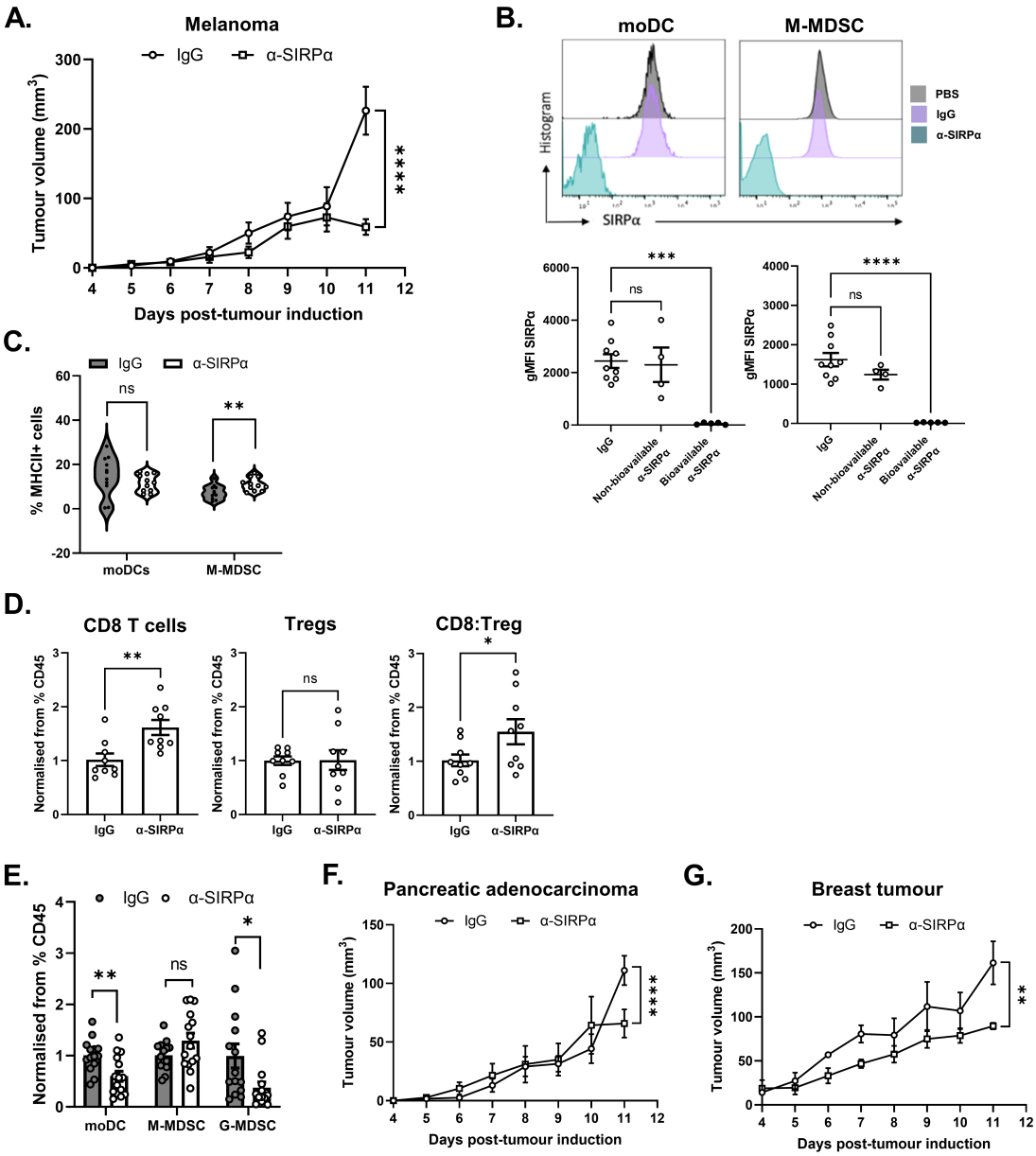
A.
Melanoma
IgG
α-SIRPα
Tumour volume (mm3)
Days post-tumour induction
****
B.
moDC
M-MDSC
PBS
IgG
α-SIRPα
Histogram
SIRPα
gMFI SIRPα
***
****
ns
IgG
Non-bioavailable α-SIRPα
Bioavailable α-SIRPα
C.
% MHCII+ cells
**
moDCs
M-MDSC
D.
CD8 T cells
Tregs
CD8:Treg
Normalised from % CD45
*
E.
G-MDSC
F.
Pancreatic adenocarcinoma
G.
Breast tumour

1187
1188

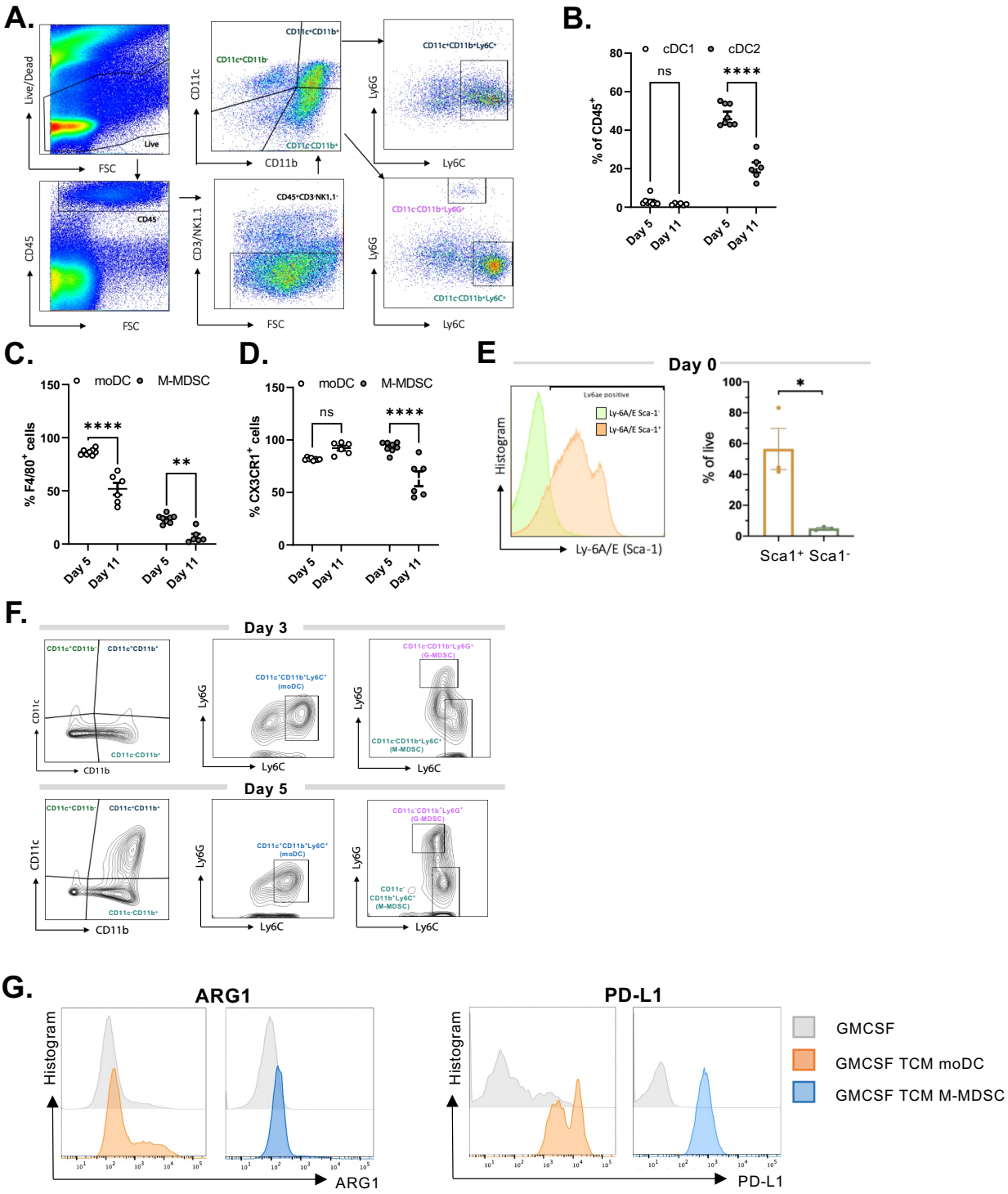

Supplementary Figure 1, Related to Figure 1-2. Characterisation of the myeloid landscape of B16-F10 tumours and in vitro. (A) Representative FACS plots of tumour at day 11 post-induction showing the gating strategy for identifying MDSCs. Live cells were gated followed by $CD3^+$ and $NK1.1^+$ cells excluded. Within $CD11c^+CD11b^+$ and $CD11c^-CD11b^+$ gates, $CD11c^+$ (moDC), $Ly6G^+$ (G-MDSC) and $Ly6C^+$ (M-MDSC) cells were identified. **(B)** Quantification of $CD11c^+CD11b^-XCR1^+$ (cDC1) and $CD11c^+CD11b^+Ly6C^-$ (cDC2) cells at day 5 and 11 post-tumour induction. Quantification of **(C)** F4/80 and **(D)** CX3CR1 expression by moDCs, M-MDSCs at day 5 and 11 post-tumour induction. **(E)** Differentiation of Sca1+ HSC *in vitro* to model myeloid landscape**;** Quantification of Sca-1 expression of HSC immediately post isolation (Day 0), and representative flow cytometry plot. **(F)** Representative flow cytometry plots from 8 independent experiments depicting gradual myeloid maturation by distribution of CD11b and C after 3 and 5 days of culture in GM-CSF. **(G)** Representative flow cytometry histograms showing ARG1 and PD-L1 expression in MoDC and M-MDSC treated with GM-CSF or GM-CSF+TCM. Data are mean ± SEM; * = $p < 0.05$, ** = $p < 0.01$, *** = $p < 0.001$, **** = $p<0.0001$. (B-D) Two-way ANOVA with a Sidak's multiple comparison post hoc test. (B) For day 5, n=4 mice and for day 11, n=3 mice performed in duplicate. (C-D) n=4 for both time points from two (day 5) and three (day 11) independent experiments.

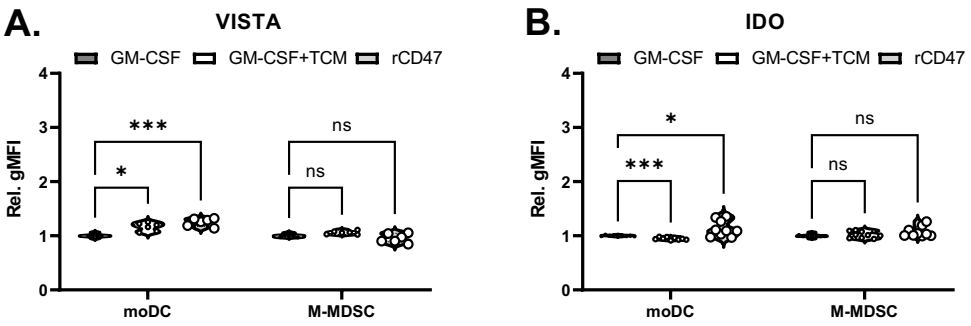

Supplementary Figure 2, Related to Figure 2. Immunomodulatory molecules expressed by MDSCs. Quantification of immune modulatory marker expression by flow cytometry shown as MFI geometric mean for **(A)** VISTA and **(B)** IDO expression in each myeloid cluster (expressed as relative gMFI normalized to GM-CSF). Data are mean ± SEM; * = $p < 0.05$, ** = $p < 0.01$, *** = $p < 0.001$, **** = $p<0.0001$. (A-B) Two-way ANOVA with a Šidák's multiple comparison post hoc test. (A-B) n=3.

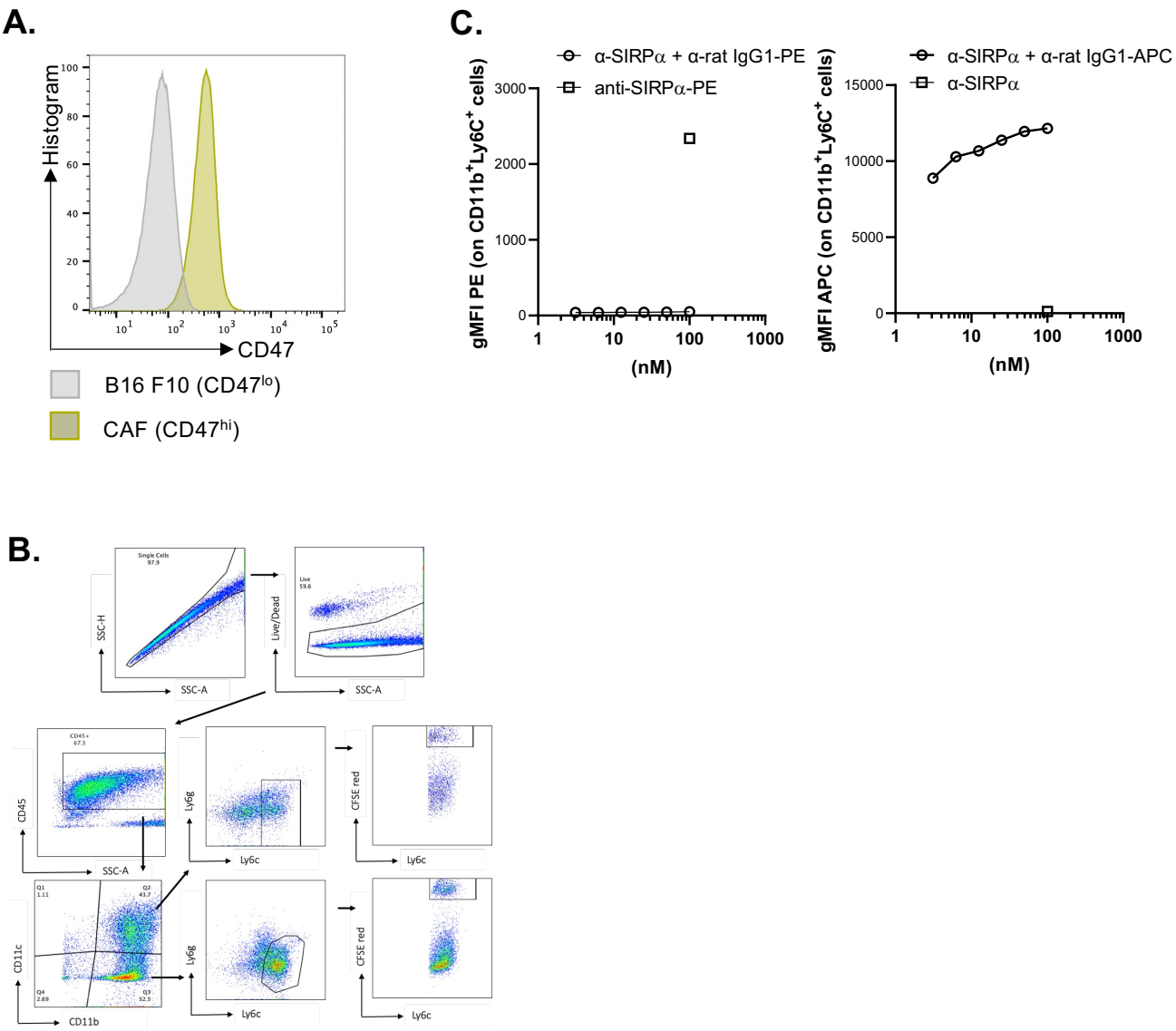

Supplementary Figure 3, Related to Figure 5. CD47-SIRPα modulation of phagocytosis and antibody binding. (A) Representative flow cytometry histogram showing CD47 expression on B16 (CD47lo and CAF CD47hi) cells. (B) Gating strategy used to analyse uptake of CFSE red stained cell debris by moDC and M-MDSC. (C) Competition assay showing occupation of SIRPα eptipoes by anti-SIRPα antibody. Left panel: Quantification of gMFI signal detected for fluorophore conjugated anti-SIRPα antibody after epitope blockade by Ultra LEAF- SIRPα antibody. Right panel: Quantification of gMFI signal detected for Ultra-LEAF antibody detected by fluorophore conjugated Rat IgG. Data are mean ± SEM; ** = $p < 0.01$, *** = $p < 0.001$, **** = $p<0.0001$. (C) n=3 independent assays performed in triplicate.

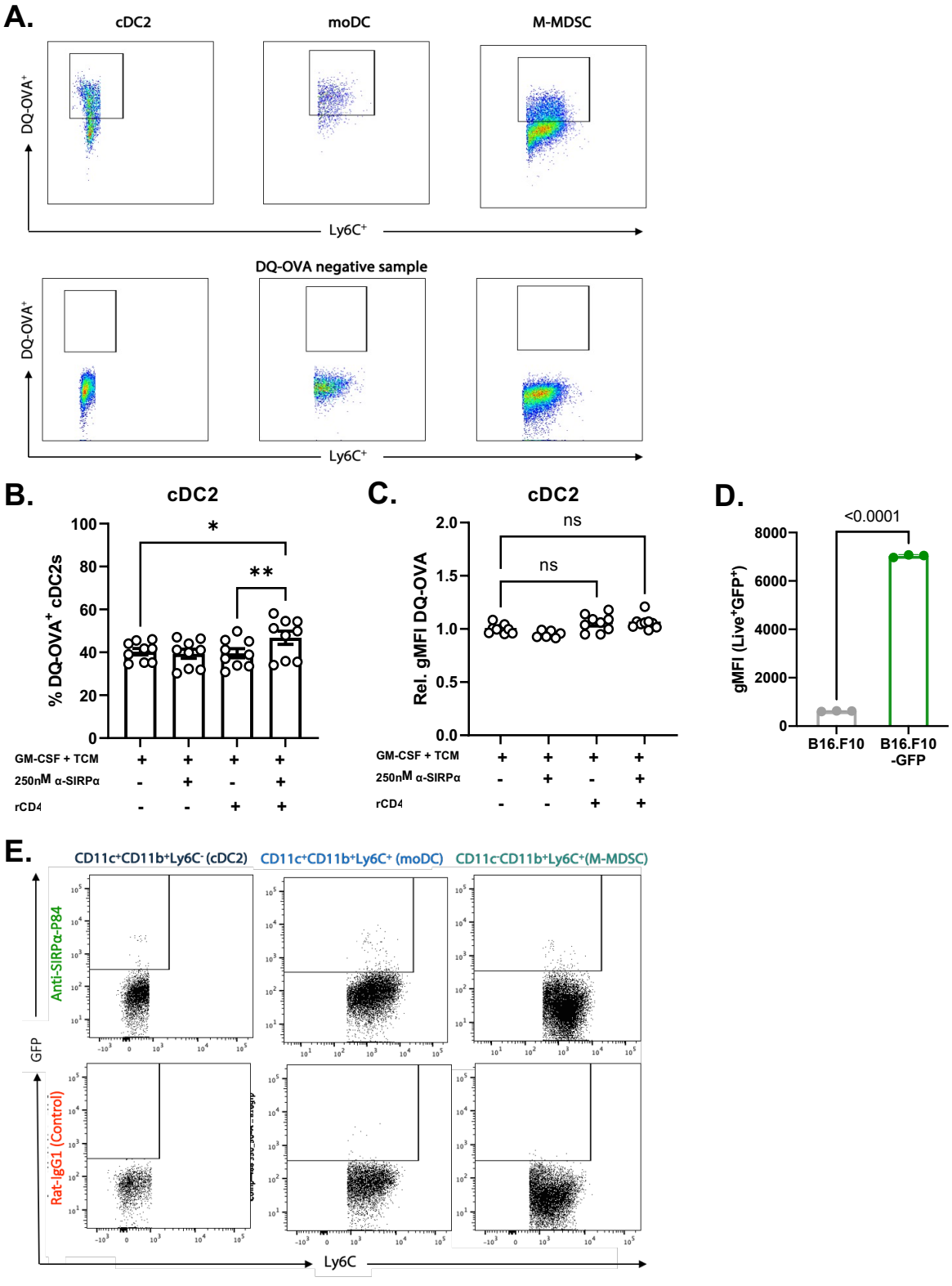

Supplementary Figure 4, Related to Figure 7. SIRPα blockade facilitates phagocytosis, antigen processing and presentation by myeloid cells. (A) Representative flow cytometry plots showing signal detected for processed DQ-OVA vs DQ-OVA negative controls in cDC2, moDC and M-MDSCs. (B) Quantification of the percentage of GM-CSF supplemented TCM treated cDC2s that uptake and proteolytic process DQ-OVA antigen with or without CD47 stimulation in the presence or absence of anti-SIRPα. (C) Quantification of the relative levels of DQ-OVA processed by cDC2s (gMFI). Data normalised to GM-CSF-TCM condition. (D) Quantification of gMFI of the GFP fluorescent protein in a stably transduced B16-F10 melanoma cell line. (E) Representative FACS showing uptake of GFP-labelled tumour material by cDC2, moDC and M-MDSC cells between anti-SIRPα injected mice and control. (Data are mean ± SEM; * = $p < 0.05$, ** = $p < 0.01$. (B-C) One-way ANOVA with Tukey's multiple comparisons and Dunnett's post hoc test, respectively. (D) Unpaired t test. (B-C) n=4 mice for each of two independent experiments.

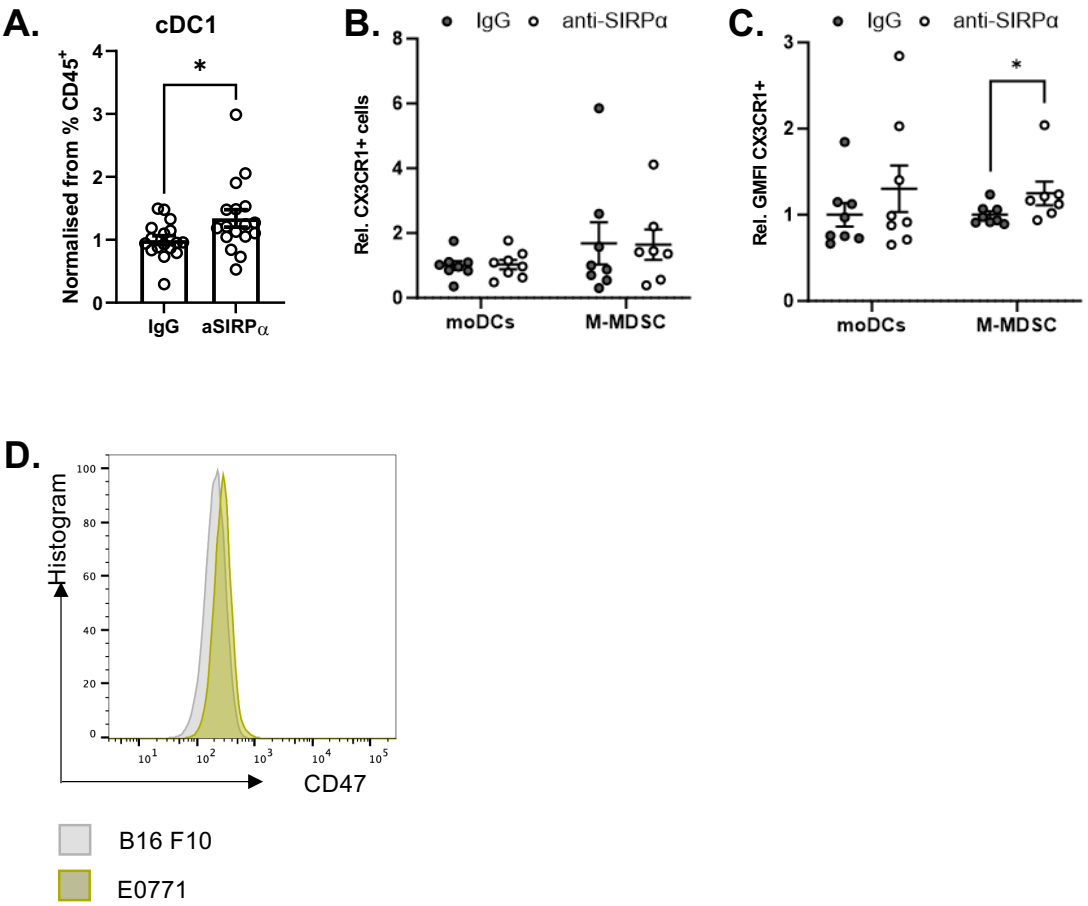

Supplementary Figure 5, Related to Figure 8. Sirpα blockade remodels myeloid composition in vivo. (A) Quantification of tumour infiltrating cDC1s (normalised to the percentage of CD45+ cells) after treatment with anti-SIRPα or isotype control. (B) Quantification of the proportion of CX3CR1+ moDCs and M-MDSC after treatment with anti-SIRPα or isotype control. Data were normalised to the rat-IgG1 controls. (C) Quantification of the expression of CX3CR1 on moDCs and M-MDSC after treatment with anti-SIRPα or isotype control. Data were normalised to the rat-IgG1 controls. (D) Representative flow cytometry plot showing comparable CD47 expression in B16F10 and E0771 breast cancer cells. Data are mean ± SEM; * = $p < 0.05$, ** = $p < 0.01$. (A-C) Unpaired t test. (A) n=3 independent experiments each with n=3 per group. (B-C) n=4 for each group from 2 independent experiments.